Integrated platform for multi-scale molecular imaging and phenotyping of the human brain

Juhyuk Park[1,2,3,6,9], Ji Wang[1,2,9], Webster Guan[3,9], Lee Kamentsky[1,2], Nicholas B. Evans[1,2], Lars Gjesteby[5], Dylan Pollack[5], Seo Woo Choi[3], Michael Snyder[5], David Chavez[5], Yuxuan Tian[3], Clover Su-Arcaro[2], Dae Hee Yun[1,2,4], Chuanxi Zhao[2], Laura Brattain[5], Matthew P. Frosch[8] and Kwanghun Chung[1,2,3,4,6,7]*

[1]Institute for Medical Engineering and Science, Massachusetts Institute of Technology (MIT), Cambridge, MA 02139, USA
[2]Picower Institute for Learning and Memory, MIT, Cambridge, MA 02139, USA
[3]Department of Chemical Engineering, MIT, Cambridge, MA 02139, USA
[4]Department of Brain and Cognitive Sciences, MIT, Cambridge, MA 02139, USA
[5]MIT Lincoln Laboratory, Lexington, MA 02421, USA
[6]Center for Nanomedicine, Institute for Basic Science, Seoul 03722, Republic of Korea
[7]Graduate Program of Nano Biomedical Engineering, Advanced Science Institute, Yonsei University, Seoul 03722, Republic of Korea
[8]C.S. Kubik Laboratory for Neuropathology, Massachusetts General Hospital and Harvard Medical School, Boston, MA 02114, USA
[9]These authors contributed equally to this work.
*Correspondence should be addressed to K.C. (khchung@mit.edu).

ABSTRACT

A detailed understanding of the anatomical and molecular architectures of brain cells and their brain-wide organization is essential for interrogating human brain function and dysfunction. Extensive efforts have been made toward mapping brain cells through various lenses, and have established invaluable databases yielding new insights. However, we still lack technologies that allow us to capture multi-scale multi-omic properties of individual brain cells in a holistic and scalable manner. To address this challenge, we developed a fully integrated technology platform for scalable three-dimensional (3D) mapping of human brain cells at subcellular resolution by simultaneously extracting brain-wide structure and high-dimensional features (e.g., spatial, molecular, morphological, and connectivity information) of individual cells from the same brain. We accomplished this by seamlessly integrating new chemical, mechanical, and computational tools to enable highly multiplexed multi-scale 3D proteomic imaging of human brain tissues with minimal information loss. We developed a novel microtome, termed MEGAtome, that enables ultra-precision slicing of a whole-mount intact human brain hemisphere and large arrays of animal organs with minimal loss of intra- and inter-slice information. To preserve structural and molecular information within intact human brain slabs and to enable highly multiplexed multiscale imaging, we developed a tissue-gel technology, termed mELAST, that transforms human brain tissues into an elastic, thermochemically stable, and reversibly expandable tissue-hydrogel. To reconstruct the intact brain to preserve the 3D connectivity information of neural fibers, we developed a semi-automatic tissue reconstruction computational pipeline termed HuBRIS. We demonstrated the utility and scalability of the technology platform by processing whole human brain hemispheres, investigating Alzheimer Disease (AD) pathology, and demonstrating the feasibility of projectome mapping.

INTRODUCTION

To fundamentally understand human brain function and dysfunction, detailed mapping of the anatomical and molecular architectures of brain cells and their brain-wide connectivity is essential[1–3]. Neuroimaging techniques (MRI, fMRI, DWI) have vastly increased our knowledge of the functional and structural organization of the human brain[4–8]. But these methods fail to capture fine structural, cellular, and molecular organization owing to the limitations in spatial resolution[9,10]. Cytoarchitectural maps, on the other hand (i.e., parcellation of the brain based on differences in cell size and density), have been around much longer. In the early twentieth century, Brodmann defined approximately 52 regions in the human cortex[11]. This cortical cytoarchitectural map is still widely referenced today, from the research bench to the neurosurgical operating theater. Cytoarchitectural maps of the human brain have been pivotal to our study of neuroscience thus far. However, they lack the critical molecular, cellular, and connectivity information required to understand cell function and complex intercellular, inter-regional interactions[9,12].

Chemoarchitectural information vastly enriches our understanding of the brain, providing a new window into the distribution of cell types, the proteins expressed, and micro-environments of each cell type. However, these histological studies are often restricted to a few markers and small regions. These studies also require sectioning the brain and thereby often suffer from loss of 3D spatial information. Additionally, most studies resort to a subsampling approach, in which serial sections are stained for different markers, and coexpression analyses are limited by the host of the antibodies and the number of channels available for imaging.

With the development of high-throughput single-cell/single-nuclear RNA-seq (scRNA-seq/snRNA-seq) technology[3,13], many more cell types can now be distinguished by their gene expression profiles. However, these methods inherently limit the acquisition of spatial information that can allow for the study of cell-to-cell interactions, co-expression, classification based on morphological details, and an overall understanding of the microenvironment at the cellular level. Advances in spatial transcriptomics have enabled systematic analysis of the cellular composition within tissue context[14]. Although these tools have dramatically advanced our understanding of the cellular landscape of the brain, they have largely been confined to animal models or surgically dissected human clinical samples due to the stringent requirement for preserving mRNAs in these methods.

Recently, much progress has been made in combining information across modalities. In 2016, a cortical brain map was released that took into account cortical thickness, brain function, the topographic organization of cells, and MRI-based measures of iron and myelin content, to further define cortical regions, averaging data from over 200 people[15]. Although this yielded new information on the structural-functional spectrum, it again did not study chemoarchitectural variation across these regions. Another study by the Allen Brain Institute in 2016 mapped the entire human brain using 50 μm-thick slices by

alternating staining for Nissl, non-phosphorylated neurofilament protein, and parvalbumin and combined this information with anatomical MRI images of the same brain[16]. This brain atlas is the first to integrate MR-based neuroimaging data with cyto- and chemoarchitectural data, thereby resulting in more thorough parcellations of brain regions and cells. However, we still lack technologies that allow us to capture multi-scale multi-omic properties of individual cells and their brain-wide connectivity.

To build upon the progress made in recent years, we developed a fully integrated scalable technology platform for establishing three-dimensional (3D) human brain cell atlas at subcellular resolution by simultaneously mapping brain-wide structure and high-dimensional features (e.g., spatial, molecular, morphological, and connectivity information) of cells acquired from the same whole brains (**Fig. 1,6**). We accomplished this by seamlessly integrating new chemical, mechanical, imaging, and computational tools to enable highly multiplexed multi-scale 3D proteomic imaging of human brain tissues. We demonstrated its utility and scalability by processing whole human brain hemispheres and investigating Alzheimer Disease (AD) pathology.

RESULTS

MEGAtome enables high precision slicing of ultra large tissues.

Microscopic interrogation of large biological systems, such as mammalian organs, is crucial in understanding structural and functional architectures of the systems. Recent development in tissue transformation techniques, such as CLARITY[17], SHIELD[18], SWITCH[19], CUBIC[20], and uDISCO[21], has made significant progress towards molecular labeling and microscopic imaging of intact animal organs without the need for mechanical sectioning by rendering intact tissue chemically permeable and optically transparent. When synergistically deployed with high-speed microscopy and long working distance (WD) objectives, these technologies have enabled holistic and high-throughput volumetric imaging of intact rodent organs at single cell resolution. However, microscopic imaging of larger samples that are thicker than the WD of available objectives, such as human brains, still requires mechanical slicing. In addition, imaging fine subcellular structures, such as cellular morphology, axonal projections, and synapses, are only possible within thin sections due to the fundamental limitations of optical hardware. On the other hand, tomographic platforms that combine serial microscopic imaging and vibratome tissue sectioning have achieved fast volumetric imaging[22,23]. However, such platforms require tissue pre-labelling, therefore, inapplicable to human organs. A method of slicing intact ultra large tissues with minimal tissue damage that allows for inter-slices co-registration is essential to achieve high-resolution 3D mapping of whole human organ-scale tissues.

Vibratome tissue sectioning remains the most efficient method for processing large tissues compared to microtome and cryostat sectioning. Biological tissues are generally too soft to be cut without being “pushed” or deformed by an advancing blade. To solve this issue, a microtome or a cryostat requires hardening of the tissue beforehand by paraffin embedding, plastic resin embedding, and sample freezing. The hardened tissue can be sectioned as thin as several microns, for electron microscopy applications for example[24], but it is difficult to generate thick and uniform slices (> 200 μm) using these methods, as thick and hardened tissue sections are prone to bend permanently during sectioning. A vibratome, on the other hand, can directly cut soft tissues thanks to its vibrating blade that applies oscillating shear cutting force to the sample. Because soft tissues are viscoelastic materials, their dynamic moduli increase as the vibrating blade exerts dynamic force on the material, leading the tissue to be “hardened” temporarily and locally by the vibration of the blade[25,26]. A vibratome is suitable for generating thicker slices (100 μm – several millimeters) and it requires much less tissue pretreatment. However, commercial vibratomes are limited to small tissues, for example, the Leica VT1200 has a maximum sample size of 33 mm [width] × 20 mm [height] × 50 mm [length]. Despite their size limit, commercial vibratomes also fail to uniformly slice highly inhomogeneous tissues due to their limited blade vibrating speed and large out-of-plane blade vibration. Ultra large-scale tissues, such as human brains, often have more significant anatomical complexity and inhomogeneity, making it more challenging to achieve continuous, uniform slicing.

To address these challenges, we developed a highly versatile vibratome, termed MEGAtome (**M**echanically **E**nhanced **G**reat-size **A**brasion-free vibra**tome**), that enables ultra-precision slicing of a wide range of biological samples from small organoids (approximately 0.5 mm in diameter) to intact human brain hemispheres (approximately 65 mm [width] × 180 mm [height] × 130 mm [length]) and large arrays of animal organs (e.g., 35 mouse brains) with minimal loss of information. MEGAtome minimizes tissue damage and maximally preserves intra- and inter-slice information by enabling high frequency blade vibration with large amplitude and low out-of-plane vibration displacement.

Analytical modeling and experimental observations have shown that the following three parameters together determine the precision and scalability of vibratome sectioning: (1) blade vibrating frequency, (2) vibrating amplitude, and (3) out-of-plane blade displacement[27–29]. A vibrating blade exerts both shear force and normal force to a soft tissue during tissue slicing. The shear force, generated by blade vibration, plays the crucial role of “breaking” the tissue at the tissue-blade contact point by creating a critical stress and strain condition in the material. The normal force, generated by blade advancement into the material, assists the formation of the stress condition by pushing the material to deform. Material deformation, e.g., tissue stretching, caused mainly by the normal force is always preferred to be minimal in tissue slicing to prevent unwanted tissue damage. Analytical modeling and experimental observations

have shown that, if the speed of the shear force is high, the critical “break” condition can be met with less normal force, meaning, intuitively, that a clean cut can be achieved by a fast blade [27–29]. For the design of a vibratome, the speed of blade vibration is proportional to the product of the blade vibrating frequency and vibrating amplitude. Therefore, high blade vibrating frequency and amplitude are desirable for slicing tissues with less tissue damage. In particular, high blade vibrating frequency is beneficial for slicing soft tissues because tissue shear deformation caused by the oscillating shear force decreases as its frequency increases.

The out-of-plane displacement of the blade is another important factor that determines the quality of soft tissue slicing and its scalability to large samples. The out-of-plane displacement is the distance that a blade moves away from its advancing plane. This unwanted blade movement causes tissue above and below the plane to be damaged by the blade, which worsens as the blade length increases. To achieve high precision slicing of large-scale tissues, it is crucial to minimize the out-of-plane displacement. Current commercial and custom vibratomes have limited blade vibrating frequency and amplitude due to their inherent design trade-off between frequency and amplitude[27,30]. Moreover, high out-of-plane blade displacement in these systems causes uneven slicing, which worsens as the tissue size increases, limiting their scalability to large-scale samples (e.g., human brain and animal organ array).

To overcome these limitations, we developed a new blade vibration generation and control mechanism that can achieve high blade vibrating frequency, high amplitude, and minimal out-of-plane displacement all together (**Fig. 2a,d,e**). The system consists of a blade mounting assembly (BMA) that can secure a 120 mm-long custom-designed blade, three pairs of flexures (F_1, F_2 and F_3) that collectively act as a single-axis motion guide and a displacement amplifier for the blade mounting assembly, a voice coil actuator (VCA) that generates an oscillating force, and two laser displacement sensors (LDS) that measure the input and output vibration displacement (**Fig. 2d**). To operate the machine, a sinusoidal current is given to the moving coil of the VCA, which then generates an oscillating force to drive the blade mounting assembly to vibrate along the x-axis (**Fig. 2e**). The blade vibrating frequency and amplitude are controlled by the frequency and amplitude of the driving current. To control the feeding movement of samples as large as 115 mm [width] × 200 mm [height] × 300 mm [length], we designed a sample mounting and feeding platform (**Fig. 2a,b**). The sample feeding speed is adjustable (0 - 50 mm/s) by controlling the speed of the motorized stage.

The multi-degree-of-freedom (multi-DOF) design (**Fig. 2f**, right) of MEGAtome can realize high blade vibrating amplitude at high frequency unlike current commercial and custom vibratomes that are based on single-DOF system design (**Fig. 2f**, left)[27,30]. In single-DOF design, vibration input is directly applied to a blade mounting assembly (*M*) which is constrained by one spring component (*K*). Such system has an inherent design trade-off between its vibrating frequency and amplitude: a system with

high spring stiffness can operate at a high frequency but low amplitude response; a system with low spring stiffness can achieve large amplitude but only at a lower frequency. On the other hand, MEGAtome's multi-DOF design is not subjected to the trade-off as its forced vibration response involves multiple design elements: two masses (M_1, M_2) and three springs (K_1, K_2, and K_3). The multi-DOF system can be modeled as a forced mass-spring vibration system that consists of two moving masse (M_1 represents the intermediate mass that is connected to the VCA, M_2 represents the mass of the blade and the blade mounting assembly) and three springs (K_1, K_2, and K_3 represent their stiffnesses, respectively). A sinusoidal force is applied to the intermediate mass M_1 to indirectly drive the blade mounting assembly M_2. Simulation results of the single- and multi-DOF systems' forced response show that when given the same oscillating force, the multi-DOF system has two natural frequencies (~88 Hz and ~145 Hz), whereas the single-DOF system has one natural frequency (**Fig. 2g**). When excited near the natural frequencies, X_1 (vibrating amplitude of M_1) and X_2 (vibrating amplitude of M_2) are significantly increased due to mechanical resonance. Taking advantage of this property, we can drive the multi-DOF system near its higher natural frequency (~140 Hz) to generate increased blade vibrating. In comparison, the single-DOF system has one natural frequency at a much lower level (~ 70 Hz), and its amplitude drastically decreases if excitation frequency higher than 70 Hz is applied (**Fig. 2g**). Therefore, the operation of the single-DOF system is limited to lower frequency and lower amplitude.

To experimentally validate our computational model, we measured the vibrating amplitude, X_1 and X_2 of MEGAtome with the two laser displacement sensors (**Fig. 2d,h**). Our results show that X_1 and X_2 are peaked at around 80 Hz (first resonant frequency) and 140 to 150 Hz (second resonant frequency), complying with the simulation results (**Fig. 2g,h**). Considering that the blade vibrating speed u ($u = \dot{x_2}(t) = X_2\omega cos\omega t$) is the product of X_2 and the driving frequency ω, the maximum blade vibrating speed is realized at 140 Hz. We next measured vibration output amplitude versus vibration input amplitude for both MEGAtome and VT1200 at their optimal operating frequencies (**Fig. 2i**). Results show that MEGAtome's blade vibrating amplitude increases linearly with its vibration input and reaches 3.4 mm peak-peak value at 140 Hz, whereas VT1200 has its best performance at 2.4 mm peak-peak value and 85 Hz. Taken together, these results demonstrate that MEGAtome overcomes the trade-off between blade vibrating frequency and amplitude and realized 2.33 times higher blade vibrating speed than VT1200 at a 1.65 times higher frequency. Importantly, given that the output amplitude X_2 equals approximately 2.5 times of the input amplitude X_1 at the operating frequency, the mechanism realized vibration amplification with small excitation input, which is preferred because mechanical errors and noise caused by the actuator, such as actuator misalignment, can be reduced.

Minimizing blade out-of-plane parasitic vibration is critical to achieve precise and scalable tissue sectioning with minimal tissue damage. In the mechanical design of MEGAtome, we minimized this out-

of-plane displacement by increasing the system's out-of-plane stiffness (**Fig. 2d,e,j**). The configuration of the flexures, particularly the vertical orientation of F_3, ensures high stiffness in out-of-plane directions, including Z, θ_x and θ_y direction. To characterize this experimentally, we used high-precision capacitance probes (CP) to measure the out-of-plane displacement of the same blade that is mounted onto both MEGAtome and VT1200. The data confirmed that the out-of-plane vibrating amplitude of MEGAtome is significantly lower than that of VT1200 even though MEGAtome operates at much higher frequency (**Fig. 2k**). Next, we compared tissue slicing performance of the two machines by slicing large human cerebellum tissues (36 mm x 45 mm x 20 mm) from the same brain into 1, 0.2, and 0.1 mm-thick sections (**Fig. 2l**). The surface profile of the 1 mm-thick sections were measured using an optical profilometer (Methods). The heat map and the photos of the sections show that MEGAtome can generate intact slices with great surface evenness without damaging the fine tissue architectures (see zoom-in photos in **Fig. 2l**). On the other hand, the single-DOF system not only generated highly uneven tissue section, but also caused severe damage of the cerebellar gyri and sulcus structures (**Fig. 2l**).

Whole mount slicing of intact human brain hemispheres and large animal organ arrays.

Recent advances in imaging (e.g., light-sheet microscopy[31]) and tissue transformation technologies (e.g., ELAST[32], DISCO[33,34]) have enabled molecular labeling and imaging of large-scale thick samples. However, due to the fundamental limitations of modern optics, maximum imageable tissue thickness is limited to the working distance (WD) of the objectives. To image large samples, such as human organs, the sample needs to be mechanically sliced to create mm-thick slices. In this process, minimizing the number of dissected tissue blocks can drastically reduce human labor, cost, and information-loss associated with sectioning, manual handing, and subsequent processing of the dissected tissues. For instance, whole mount sectioning of an entire human brain hemisphere into intact 4-mm-thick coronal slabs is highly desirable because it generates only 40-50 slabs, whereas slicing the same brain into cube-shaped tissue blocks with the equal thickness produces thousands of pieces that are difficult to track and process without substantial human labor and resources. No vibratomes available, however, can realize whole-mount precision slicing of human-organ scale tissues. The challenges lie in not only the large size of the human organs, but also its complicated structure and highly inhomogeneous material properties that small samples lack. For example, in a human brain, tough meninges can be buried deep in the sulci and surrounded by delicate grey matter. It is required for the vibratome to cut through these areas without dragging meninges into the grey matter thus causing damages. A human brain also has large internal ventricles, around which materials are not well supported or constrained from deforming during slicing, thus adding to the challenge of precision slicing.

Despite these challenges, MEGAtome was able to slice a whole-mounted human brain hemisphere and generate continuous, uniform and intact 4 mm-thick coronal slabs in a highly scalable manner (**Fig. 3a-c,e**). To whole-mount the human brain hemisphere and secure it during repeated slicing cycle, we first poured liquid gel onto the hemisphere in a custom-designed container that has detachable walls (**Fig. 3d**). After the gel became solidified, walls of the container were detached. The gel block was submerged in 4% formaldehyde solution for seven days until sufficient bonding was formed between the tissue and the gel, followed by washing in PBS solution. Finally, the hemisphere was mounted onto MEGAtome for slicing in coronal position. One slicing cycle takes 7-10 minutes and it takes only 8 hours to cut an entire hemisphere into 40 four mm-thick slabs. **Figure 3e** shows 40 consecutive 4 mm-thick coronal blocks from a whole human brain hemisphere successfully sliced with MEGAtome. Being able to establish well-preserved mm-thick tissue slabs with minimal loss of inter- and intra-slab information enables downstream imaging of a whole 3D human brain hemisphere volume at subcellular resolution within 100 hours (**Fig. 3f,g**) and co-registration of the 3D datasets at single fiber resolution (**Fig. 7i**). Considering the human brain is one of the most complicated and largest human organs, we believe MEGAtome is suitable for whole-mount precision slicing of other human organs, such as kidney, heart, etc. for rapid, scalable, high-resolution molecular imaging.

MEGAtome can also synergize with the pioneering tissue processing and imaging technologies to enable rapid and highly scalable molecular imaging of cohort-scale animal organs. Accelerated development of new genetic animal models and large-scale studies have greatly increased the need for imaging a large number of animal brains in a high-throughput and cost-effective manner. However, the current approaches rely on manual handling of individual samples in a piecemeal manner that not only limits the throughput, but also increases human labor, cost, and sample-to-sample variations. As a first step to address this challenge, we developed a device and protocol that can create MEGAtome-compatible high-density sample arrays for high-throughput parallel processing and imaging of a wide range of biological samples. To maximize the slicing and imaging efficiency, we wanted to ensure that each sample is positioned in the same exact orientation with minimal spaces in between. To realize this, we custom-designed embedding tools that consist of a container with detachable walls, animal organ-shaped placeholders, and a patterned rack that fits 5x7 placeholders (**Fig. 3h**). To use the tools for mouse brain array gel-embedding, we first assemble the tools and then pour a liquid gel solution to the container. The mouse brain-shaped placeholders allow the gel to form a fitted mold to hold each brain in the same orientation. Once the gel is solidified, placeholders are removed, and 35 mouse brains are placed in the gel mold. More liquid gel is then poured to fully immerse the brains. After the gel solidifies, the brain-gel array is fixed by PFA to crosslink with the tissue. Using MEGAtome, we were able to generate uniform mouse brain array slices in 100 μm - 2 mm thickness (**Fig. 3m**). Based on the same idea of mouse brain

array embedding, we demonstrated embedding and slicing of an array of 6 marmoset brain hemispheres. The marmoset brain hemisphere-shaped placeholder was designed based on the 3D surface scan of a marmoset brain left hemisphere (**Fig. 3n**). In summary, we report the design of MEGAtome that realized precision slicing of ultra-large systems with minimal loss of intra- and inter-slice information. The mechanical design of MEGAtome overcame the trade-off between blade vibrating frequency and vibrating amplitude that limits the performance of state-of-the-art machines. The flexure based multi-DOF system design amplifies blade vibrating speed at high frequency, and at the same time minimizes the blade mechanical errors that are detrimental to tissue slicing. The synergistic gel embedding protocol and MEGAtome slicing facilitates high-throughput imaging of ultra-large-scale brain samples at multiple scales.

mELAST enables multi-scale multiplexed molecular imaging of human brain tissues.

To preserve structural and molecular information of the human brain tissues and to enable highly multiplexed multiscale imaging, we developed an integrated tissue transformation pipeline by combining SHIELD[18], ELAST[32], and MAP[35]. SHIELD controls diffusion-reaction kinetics of epoxide-based fixatives to yield homogeneous preservation of molecules and tissue architecture (**Fig. 4a**). Proteins can be permanently preserved in fully delipidated SHIELD-tissue during repeated staining, imaging, and destaining cycles (**Supplementary Fig. 3**). After SHIELD treatment, mELAST (MAP-ELAST) transforms tissues into an elastic, thermochemically stable, and reversibly expandable tissue-hydrogel (**Fig. 4a,b** and **Supplementary Fig. 1a-f**)[32,35]. By engineering a synthetic hydrogel with highly entangled and super-absorbent polymeric chains for hybridizing biological tissues[36], we were able to achieve 4.5-fold linear expansion in DI water while keeping the tissue-gel elastic and indestructible (**Fig. 4b,c** and **Supplementary Fig. 2a,b**). Once mELAST processing is done, we photobleach the expanded mELAST sample to enable high signal-to-noise imaging by removing endogenous autofluorescence (e.g., lipofuscin) found in human brain tissues and other organs. We built a human brain-scale tissue photobleaching device and established protocols that can uniformly photobleach tissue autofluorescence (**Fig. 4d-f** and **Supplementary Fig. 4)**. Because expanded mELAST tissue-gel is sufficiently transparent, we were able to drastically reduce tissue autofluorescence uniformly throughout the thick tissue-gel and achieve high signal to noise ratio (SNR) data acquisition (**Figs. 4e,f, 5, 7**).

To achieve rapid and uniform immunostaining of SHIELD-mELAST tissue-gels in a cost-effective way, we developed a SWITCH-Pumping protocol (**Supplementary Fig. 2d**). This protocol utilizes a custom-designed, human-brain-scale, pump device that enables highly reproducible mechanical tissue thinning by the relative linear movement between a pump head and a flat-bottomed container that encloses mELAST-processed tissues and labeling solutions (**Fig. 4g**). The tissue pump accelerates

probe delivery by reducing the characteristic tissue thickness and creating convective flow via cyclic mechanical compressions (**Fig. 4g,h**). During the cyclic compression, we modulate antibody-antigen binding reactions using SWITCH[19] to prevent depletion of antibodies along the tissue surface and enhance antibody penetration. This SWITCH mediated tissue pumping allows us to drastically reduce the amount of antibodies required for staining large human tissue while improving the staining uniformity even for highly expressed targets, such as Parvalbumin (PV), Neurofilament heavy chain (NFH), and SMI-312 (a pan-axonal marker) (**Fig. 4h,j,k**). The operation of the pump device is automated, ensuring reproducible and scalable tissue labeling. Using the SWITCH-Pumping strategy, we not only achieved 1-day uniform primary staining (anti-CR and SST antibodies) of 2.5-mm-thick whole human coronal mELAST slabs, but also the very dense SMI-312+ axonal fibers in mm-thick tissue could be stained homogeneously, with a small amount of antibodies (**Fig. 4j,k**).

To image the large volume of human brain tissues, we have developed multicolor Inverted Axially-Swept Light-Sheet Fluorescence Microscopes (IASLSFM, **Fig. 4i**) with the capacity to capture multiscale data with objectives ranging from 2x to 25x at near isotropic resolution (**Supplementary Table 2**). For full human brain slab imaging at cellular resolution, a 2x/0.1NA objective provides long working distances up to ~12 mm of depth. Each microscope is equipped with a continuous wavelength, multicolor laser source which operates at 405, 488, 561, 647, and 785 nm wavelengths. Two different custom-designed microscope stages can accommodate tissue dimensions of up to 180 x 380 mm, enabling super-resolution imaging of the expanded whole human brain coronal hemi slab. With IASLSFM, we can achieve high axial resolution with near-isotropic voxel size as well as high speed line-scanning detection. With a proper choice of the detection objective, we were able to resolve not only individual cells but fine subcellular features such as axons and dendrites (**Fig. 4i,k**). **Figure 3f,m** shows a 4 mm-thick intact human brain coronal slab (110 mm x 75 mm) that contains multiple cortices, thalamus, and hippocampus regions and a 2 mm-thick mouse brain array (98 mm x 72 mm). After NeuN staining, we imaged the whole slab and the array with IASLSFM and the 2x objective only within 6 hours and 4 hours, respectively, capturing the ultra-large-scale 3D distribution of NeuN+ cells at single cell resolution (**Fig. 3g,m**). Using one IASLSFM system, the whole brain hemisphere volume can be imaged at single cell resolution approximately within 100 hrs. The system equipped with a 16.7x/0.4NA objective (15x magnification) can also be used for imaging expanded tissues at single-axonal resolution (**Fig. 4k**). Together, this powerful and robust imaging system combined with mELAST technology allows us to perform high-throughput multiscale imaging of human brain-scale tissues based on tissue expansion and objective choices.

3D multi-scale proteomic interrogation of control and AD human brain tissues.

We applied the platform for interrogating molecular and structural details of human Alzheimer disease at multiple scales (**Fig. 5**). Two human brain coronal slabs with and without Alzheimer Disease (AD) pathology were processed and imaged. For the first round of staining, each slab was stained using nuclear dye and antibodies targeting NeuN and IBA1. The pan-neuronal marker NeuN facilitates cytoarchitectural parcellations. The nuclear marker enables detection of all nuclei and is used for co-registration of multi-round datasets at single cell resolution. IBA1 visualizes largely the microglia population. After staining and index matching, the slabs were volumetrically imaged with the IASLSFM system equipped with a 2x objective. The imaged slabs were destained, restained with the next set of markers, and reimaged. Neuronal cell-type markers (PV, Calretinin [CR], Neuropeptide-Y [NPY], somatostatin [SST]), glia markers (Iba1, Glial fibrillary acidic protein [GFAP]), and pathogenic protein markers (Beta amyloid, Phosphorylated Tau) were used for multi-round staining (**Supplementary Fig. 6**). During this entire process, the unprecedented mechanical and chemical stability of the mELAST tissue-gel allowed the sample to withstand the repeated destaining and pumping labeling cycles without tissue damage. The four rounds of images were processed, stitched, and co-registered based on the nuclei signal from YOYO-1 at single cell resolution (**Fig. 5b**). The NeuN+ and IBA1+ cells were counted from A9m (prefrontal cortex), A11m (orbitalfrontal cortex), and MFC (cingulate neocortex) and their densities were normalized by the cortical layer thickness (**Fig. 5e,f**). As expected, the densities of IBA1+ cells in all the cortex of the AD brain were higher than those of the normal brain, whereas the densities of NeuN+ neurons were lower in the AD brain[37]. All inhibitory neuronal cell types (CR+, SST+, PV+, NPY+), particularly PV+ and CR+ cells, show significantly lower density in the AD brain tissue.

Next, we performed super-resolution investigation of the mELAST samples to characterize the loss of synaptic clusters in AD. mELAST effectively preserves tissue microenvironment, fine cell morphologies, and nanoscopic architectures during the repeated cycles of single-cell resolution investigation. The probed mELAST tissue-gel at low resolution can be restained, physically expanded, and reimaged with higher NA objectives to investigate finer subcellular architectures (e.g., neurites and synaptic clusters) within the same brain tissue (**Fig. 5g-i**). This unique advantage of mELAST allows multi-scale 3D imaging and phenotyping of the same tissue in a fully integrated manner. To interrogate the loss of synaptic clusters in AD, we stained the cortex regions (A46v, ventral subdivision of area 46 from prefrontal cortex) of the normal and AD mELAST human brain tissues with antibodies targeting beta amyloid, PSD-95 (a postsynaptic marker), and Synapsin I/II (a presynaptic marker). The stained tissues were expanded and imaged using a 63x objective. The density of the PSD95+ and Synapsin I/II+ clusters were measured. As expected, the number density of the synaptic clusters was significantly lower in AD, particularly inside beta amyloid plaques (**Fig. 5h-j**).

Computational tools for single-axon level inter-slab registration and tracing.

Mapping the brain connectome is one of the most sought-after challenges in neuroscience. Recent advances in tissue clearing and imaging technologies have enabled the visualization of large-scale neural tissue at axonal resolution at unprecedented speed. However, at the scale of intact human brains, tissue processing and high-resolution imaging remain infeasible. This necessitates the slicing of the human brain into slabs, which requires a computational pipeline that can register multiple slabs to reconstruct the intact tissue volume and to preserve the 3D connectivity information of axons and neural fibers across mechanically sliced tissues. Previous methods for computational tissue reconstruction tend to work with thin, undeformed, and laterally small tissue sections which are unscalable to large scale mammalian cortical, spinal cord, or whole coronal slab data. As such, reconstructing thick tissue accurately at axonal-resolution or at large scales has yet to be accomplished.

To address these challenges, we developed a semi-automatic tissue reconstruction computational pipeline termed **Hu**man **B**rain **R**egistration: **I**nter-**S**lab (HuBRIS), which can accurately align features at the macro-scale, meso-scale (blood vessels), and micro-scale (axons) levels. Intensity-based (e.g., optimization of a normalized cross-correlation loss function) or feature-based registration methods (e.g., Harris corner detector) used for more standard 2D image registration applications do not scale well to interslab registration of large, thick, highly-processed, and immunostained tissue. Thus, to achieve accurate interslab registration at the macro- and micro-scale, more relevant and reliable features are required. To this end, HuBRIS takes advantage of fluorescent labelling of vasculature to match blood vessel endpoints at the cut surface in order to define a smooth deformation field for intact tissue reconstruction. Blood vessels are ideal features to use for inter-slab registration due to their long-range continuity and connectivity, high signal-to-noise ratio staining profile from lectin dyes compatible with most tissue clearing protocols, as well as their dense, ubiquitous distribution throughout the brain. By ensuring vessel connectivity throughout consecutive tissue slabs, good macroscopic alignment of the two slabs can be achieved. Furthermore, to achieve true neural fiber-resolution registration and connectivity within dense fibers, a variety of fine landmarks are required throughout the tissue. By using our scalable tissue processing, staining, and imaging pipeline (**Fig. 6a**) capable of acquiring highly multiplexed data at neural fiber resolutions, we can thus feasibly use multiple fiber-labelled cell type markers to iteratively refine our interslab registration. In particular, by immunostaining our tissue with a selection of specific cell-type (such as PV and GFAP) and neurofilament protein markers (such as NFH), we can ensure comprehensive connectivity throughout two cut slabs at an unprecedented level unachievable through genetic labelling or lower resolution imaging.

HuBRIS utilizes the following steps for registering any pair of consecutive tissue slabs at vessel resolution (**Fig. 6b**): (1) image pre-processing and illumination correction, (2) surface detection, (3)

flattening of the tissue based on detected surfaces, (4) manual identification of “anchor points” (usually of large and prominent arteries) in each slab that match up to define a rough rigid alignment between the two flattened slabs, (5) surface vessel endpoint detection through the use of a vesselness filter, segmentation, and then masking to isolate surface endpoints using the mask detected in step (2), (6) feature matching of endpoints (detected in step 5) between the two surfaces based on a geographic keypoint descriptor and subsequent outlier removal, (7) thin plate spline deformation of moving image to fuse the volumes, (8) additional manual annotation of endpoints in the newly transformed frame, (9) iteratively perform steps (7)-(8) on the warped images to get progressively better connectivity alignment between the two slabs. This semi-automated process can be used to get arbitrarily good registration between consecutive tissue slabs at vasculature resolution (**Fig. 7a**).

Since vasculature is not sufficiently dense to achieve the single-axon resolution registration required for comprehensive projectome mapping and axon tracing, cell type markers that stain for fibers and neurites are needed. The vasculature deformation field is first used for macroscopic and vessel-resolution registration before the fiber endpoints of other cell type markers such as GFAP, PV, and NFH are used to refine the registration results at the fiber-scale (**Fig. 6c**). We demonstrated that HuBRIS can achieve macroscopic registration using blood vessels (**Fig. 7a**), and the registration can then be progressively fine-tuned by including the endpoints of more markers (**Fig. 7b-e**). The connectivity of individual NFH axons through the cut section of the tissue sections become progressively more accurate as more landmarks from different cell type markers are added (**Fig. 7h**). The connectivity of sparse astrocytic GFAP+ fibers is also improved by this multi-stage registration approach (**Fig. 7b-e**). The mean error magnitude of NFH-connectivity after the vasculature-based registration is 20.8 microns; after addition of GFAP and PV landmarks the mean error magnitude is 7.85 microns, and after the final addition of NFH landmarks the mean error magnitude decreases to 2.35 microns (**Fig. 7f**). The distribution of X and Y NFH connectivity error also shrinks from a spread of 10 microns (in each lateral dimension) after lectin registration, to ~5 microns after PV/GFAP registration, and finally to ~1 micron after NFH registration (**Fig. 7g**).

Automated and semi-automated neuron tracing and segmentation algorithms have previously been developed to analyze high resolution images of single neurons or sparsely labelled groups of neurons[38–40]. These algorithms are optimized primarily for two types of tasks: (1) subcellular segmentation and tracing at the nanoscale in EM images, or (2) reconstruction of single neuron morphology, enabling fine analysis of the dendritic arborization of genetically labelled single neurons. While these algorithms are suitable for tracing high resolution, high SNR, sparsely-labelled light microscopy images, to the best of our knowledge, there are no algorithms available that have shown high

accuracy axonal tracing in densely immunostained tissue volumes. Towards this end, we have developed a deep-learning axon segmentation and tracing algorithm based on the U-Net[41].

The U-Net architecture consists of 3D convolutional layers interspersed with strided max-pooling to form sequentially downsampled, lower-resolution modules in an encoder path, followed by upsampling using strided transpose convolutions with max-pooling to restore the original resolution in a decoder path, with lateral skip connections between same resolution encoder and decoder modules. Summation joining was chosen for skip connections with an additional skip connection between the first and last convolutional layer in each module. To perform end-to-end centerline detection, we implemented a centerline-Dice (clDice) loss function[42], which allows us to incorporate parameter-free skeletonization directly into the optimization process (**Fig. 6d**).

The interslab registration and automated axon tracing algorithms enabled the reconstruction of two consecutive slabs at axonal resolution and seamless connection of axons across cut surfaces (**Fig. 7i**). Multiple long fibers that traverse the two tissue slabs were reconnected and traced without truncations (**Fig. 7i**). Combined with our histological and imaging platforms, this shows that our computational pipeline of interslab registration and axon tracing is accurate, scalable, and capable of enabling large scale projectome mapping of human brain tissues.

DISCUSSION

Current tissue processing and imaging methods, elegant and pioneering as they are, do not allow fully integrated multiplexed molecular profiling of individual cells and their spatial organization in human brain-scale tissues. As a first step in addressing this limitation, we developed a host of new techniques that transform intact brain tissues into an indestructible and transparent framework, which can be repeatedly labeled and imaged. The integrated SHIELD-mELAST platform preserves endogenous proteins and their immunoreactivity, and nanoscopic tissue architecture in thick human brain slabs while allowing multiscale molecular imaging. The unprecedented mechanical and chemical stability of the tissue-gel enables many rounds of labeling, imaging, and delabeling of the same tissue without loss of information. The tissue-gel can be permanently stored and reimaged whenever additional rounds of molecular phenotyping with new markers are required. This unique feature maximizes the utility of the rare and highly important human brain tissues. It also enables the resulting atlas to continuously evolve beyond the scope of individual projects as one can continue to add more molecular, structural, and connectivity information from the same brains to the atlas. In addition, we demonstrated that SWITCH-pumping of mELAST tissue-gel can increase the rate of molecular transport by orders of magnitude, enabling exceptionally uniform immunostaining of mm-thick human brain tissues with a small amount of

antibodies. SHIELD-mELAST will enable newly integrated approaches for a wide range of neuroscience research and beyond.

Determining neural circuit connectivity at a cellular level can provide long-sought insight into the essential character of brain function and dysfunction. Yet, mapping cellular connectivity in the human brain remains impossible because the current powerful circuit interrogation techniques (e.g., viral labeling) are only applicable to experimental animals. We, for the first time, demonstrated reconstruction of inter-slab axonal connectivity at single-fiber resolution in the human brain tissues by integrating MEGAtome, mELAST, and the computational technologies. We envision that the accuracy of reconstruction and tracing will continue to improve as we increase the dimensionality of the integrated 3D datasets by adding additional rounds of 3D fiber-resolution images. The comprehensive circuit mapping enabled by the technology platform will enable the identification of non-canonical connections for better understanding of human brain circuitry.

In summary, we seamlessly combined multiple novel technologies to establish an integrated platform that enables scalable and fully integrated structural and molecular phenotyping of cells in human-brain-scale tissues at unprecedented resolution and speed. We envision that this scalable technology platform will allow us to process and analyze a large number of human brains to adequately cover human demographic diversity, individual variability, and disease spectrum. Such large-scale effort will establish the most comprehensive 3D human brain map to date that may radically alter our understanding of the human brain and thus disease mechanisms and spur development of new therapies.

Acknowledgements

We thank the entire Chung laboratory for support and discussions. K.C. was supported by the Burroughs Wellcome Fund Career Awards at the Scientific Interface, Searle Scholars Program, Packard award in Science and Engineering, NARSAD Young Investigator Award, McKnight Foundation Technology Award. This work was supported by JPB Foundation (PIIF and PNDRF), NCSOFT Cultural Foundation, and NIH (1-DP2-ES027992, U01MH117072). K.C. and J.P. were supported by the Institute for Basic Science (IBS-R026-D1). J.W. was supported by postdoctoral fellowships from the Picower Institute of Learning and Memory. W.G. was supported by the National Science Foundation Graduate Research Fellowship under Grant No. 1122374. M.P.F. was partially supported by NIA P50 AG005134. Resources that may help enable general users to establish the methodology are freely available online (http://www.chunglabresources.org). The cartoon in Figure 1 was created with BioRender.com. K.C. is a co-founder of LifeCanvas Technologies, a startup that aims to help the research community adopt technologies developed by the Chung Laboratory.

Author contributions

J.P., J.W., W.G. and K.C. conceived the idea and designed the experiments. J.P., J.W., W.G, and K.C. designed the integrated human brain phenotyping platform and wrote the paper with input from other authors. J.W. developed and characterized MEGAtome. J.W. developed the brain array method. J.W. developed the brain embedding method with help from J.P. J.W. sliced the human brain hemispheres and brain array using MEGAtome. J.P. stained and imaged the brain array and human brain slab in Fig. 3. J.P. developed mELAST technology. J.W. developed tissue pumps and photobleachers. J.P. developed the SWITCH-Pumping protocol. S.W.C. and J.P. developed the SHIELD protocol for human brain coronal slabs. J.P. performed SHIELD-mELAST processing of human brain tissues. N.B.E. developed IASLSFM. J.P. performed multi-round staining and imaging of the tissues using IASLSFM. L.K. developed the computational pipeline for processing IASLSFM images and co-registration of multi-round images. J.P. performed quantitative analyses of cells and synapses. J.P. performed super-resolution imaging. W.G. developed HuBRIS. W.G. performed multiscale interslab stitching using HuBRIS. L.G., D.P., M.S., D.C. and L.B. developed the deep learning-based axon tracing algorithm and performed axon tracing on datasets with help from W.G. J.P. imaged the human brain tissues for HuBRIS and axon tracing. Y. T. conjugated SeTau647 with secondary antibodies. J.P. screened and validated antibodies with help from D.H.Y. J.P. perfused the mouse. J.P. formulated the RI-matching media. C.S.-A. helped buffer preparation. C.Z. helped assemble tissue pumps and photobleachers. M.P.F. provided the human brain tissue specimens. K.C. supervised all aspects of the work.

Competing interests

K.C. is a co-inventor on patent application owned by MIT covering the SHIELD and SWITCH technology (PCT/US2016/064538), the MAP technology (US Provisional Patent Application 62/330,018), and the ELAST technology (US Patent App. 17/308,462). K.C. and J. W. are co-inventors on patent application owned by MIT covering the MEGAtome technology. K.C. is a co-founder of LifeCanvas Technologies, a startup that provides solutions for 3D tissue processing and analysis.

References

1. Biswal, B. B. *et al.* Toward discovery science of human brain function. *Proceedings of the National Academy of Sciences of the United States of America* **107**, 4734–4739 (2010).
2. Bassett, D. S. & Gazzaniga, M. S. Understanding complexity in the human brain. *Trends in Cognitive Sciences* **15**, 200–209 (2011).
3. Hawrylycz, M. J. *et al.* An anatomically comprehensive atlas of the adult human brain transcriptome. *Nature 2012 489:7416* **489**, 391–399 (2012).
4. Glover, P. & Bowtell, R. MRI rides the wave. *Nature 2009 457:7232* **457**, 971–972 (2009).
5. Evans, A. C., Janke, A. L., Collins, D. L. & Baillet, S. Brain templates and atlases. *NeuroImage* **62**, 911–922 (2012).
6. Amunts, K. *et al.* Interoperable atlases of the human brain. *NeuroImage* **99**, 525–532 (2014).
7. Fischl, B., Sereno, M. I., Tootell, R. B. H. & Dale, A. M. High-Resolution Intersubject Averaging and a Coordinate System for the Cortical Surface. *Hum. Brain Mapping* **8**, 272–284 (1999).
8. Fischl, B. & Dale, A. M. Measuring the thickness of the human cerebral cortex from magnetic resonance images. *Proceedings of the National Academy of Sciences of the United States of America* **97**, 11050–11055 (2000).
9. Amunts, K. & Zilles, K. Architectonic Mapping of the Human Brain beyond Brodmann. *Neuron* **88**, 1086–1107 (2015).
10. Caspers, S., Eickhoff, S. B., Zilles, K. & Amunts, K. Microstructural grey matter parcellation and its relevance for connectome analyses. *NeuroImage* **80**, 18–26 (2013).
11. K. Brodmann. Allgemeine Neurologie. in *Handbuch der neurologie* 206–307 (Julius Springer, 1910).
12. Zilles, K. *et al.* Architectonics of the human cerebral cortex and transmitter receptor fingerprints: reconciling functional neuroanatomy and neurochemistry. *European Neuropsychopharmacology* **12**, 587–599 (2002).
13. Miller, J. A. *et al.* Transcriptional landscape of the prenatal human brain. *Nature 2014 508:7495* **508**, 199–206 (2014).
14. Chen, K. H., Boettiger, A. N., Moffitt, J. R., Wang, S. & Zhuang, X. Spatially resolved, highly multiplexed RNA profiling in single cells. *Science* **348**, (2015).

15. Glasser, M. F. *et al.* A multi-modal parcellation of human cerebral cortex. *Nature 2016 536:7615* **536**, 171–178 (2016).
16. Ding, S. L. *et al.* Comprehensive cellular-resolution atlas of the adult human brain. *Journal of Comparative Neurology* **524**, 3127–3481 (2016).
17. Chung, K. *et al.* Structural and molecular interrogation of intact biological systems. *Nature 2013 497:7449* **497**, 332–337 (2013).
18. Park, Y. G. *et al.* Protection of tissue physicochemical properties using polyfunctional crosslinkers. *Nature Biotechnology 2018 37:1* **37**, 73–83 (2018).
19. Murray, E. *et al.* Simple, Scalable Proteomic Imaging for High-Dimensional Profiling of Intact Systems. *Cell* **163**, 1500–1514 (2015).
20. Susaki, E. A. *et al.* Whole-Brain Imaging with Single-Cell Resolution Using Chemical Cocktails and Computational Analysis. *Cell* **157**, 726–739 (2014).
21. Pan, C. *et al.* Shrinkage-mediated imaging of entire organs and organisms using uDISCO. *Nature Methods 2016 13:10* **13**, 859–867 (2016).
22. Ragan, T. *et al.* Serial two-photon tomography for automated ex vivo mouse brain imaging. *Nature Methods 2012 9:3* **9**, 255–258 (2012).
23. Seiriki, K. *et al.* Whole-brain block-face serial microscopy tomography at subcellular resolution using FAST. *Nature Protocols 2019 14:5* **14**, 1509–1529 (2019).
24. Graham, L. & Orenstein, J. M. Processing tissue and cells for transmission electron microscopy in diagnostic pathology and research. *Nature Protocols 2007 2:10* **2**, 2439–2450 (2007).
25. Li, W., Shepherd, D. E. T. & Espino, D. M. Dynamic mechanical characterization and viscoelastic modeling of bovine brain tissue. *Journal of the Mechanical Behavior of Biomedical Materials* **114**, 104204 (2021).
26. Rashid, B., Destrade, M. & Gilchrist, M. D. Mechanical characterization of brain tissue in compression at dynamic strain rates. *Journal of the Mechanical Behavior of Biomedical Materials* **10**, 23–38 (2012).
27. Wang, J., Li, C. & Chen, S. C. Sectioning soft materials with an oscillating blade. *Precision Engineering* **56**, 96–100 (2019).
28. Mora, S. & Pomeau, Y. Cutting and Slicing Weak Solids. *Physical Review Letters* **125**, 038002 (2020).
29. Reyssat, E., Tallinen, T., le Merrer, M. & Mahadevan, L. Slicing softly with shear. *Physical Review Letters* **109**, 244301 (2012).
30. Jiang, T. *et al.* A platform for efficient identification of molecular phenotypes of brain-wide neural circuits. *Scientific Reports 2017 7:1* **7**, 1–12 (2017).
31. Wu, Y. *et al.* Inverted selective plane illumination microscopy (iSPIM) enables coupled cell identity lineaging and neurodevelopmental imaging in Caenorhabditis elegans. *Proceedings of the National Academy of Sciences of the United States of America* **108**, 17708–17713 (2011).
32. Ku, T. *et al.* Elasticizing tissues for reversible shape transformation and accelerated molecular labeling. *Nature Methods 2020 17:6* **17**, 609–613 (2020).
33. Ertürk, A. *et al.* Three-dimensional imaging of solvent-cleared organs using 3DISCO. *Nature Protocols 2012 7:11* **7**, 1983–1995 (2012).
34. Renier, N. *et al.* iDISCO: A Simple, Rapid Method to Immunolabel Large Tissue Samples for Volume Imaging. *Cell* **159**, 896–910 (2014).
35. Ku, T. *et al.* Multiplexed and scalable super-resolution imaging of three-dimensional protein localization in size-adjustable tissues. *Nature Biotechnology 2016 34:9* **34**, 973–981 (2016).
36. Choi, S. W., Guan, W. & Chung, K. Basic principles of hydrogel-based tissue transformation technologies and their applications. *Cell* **184**, 4115–4136 (2021).
37. Shepherd, C. E. *et al.* Alzheimer's amyloid-β and tau protein accumulation is associated with decreased expression of the LDL receptor-associated protein in human brain tissue. *Brain and Behavior* **10**, e01672 (2020).
38. Quan, T. *et al.* NeuroGPS-Tree: automatic reconstruction of large-scale neuronal populations with dense neurites. *Nature Methods 2016 13:1* **13**, 51–54 (2015).
39. Winnubst, J. *et al.* Reconstruction of 1,000 Projection Neurons Reveals New Cell Types and Organization of Long-Range Connectivity in the Mouse Brain. *Cell* **179**, 268-281.e13 (2019).
40. Banerjee, S. *et al.* Semantic segmentation of microscopic neuroanatomical data by combining topological priors with encoder–decoder deep networks. *Nature Machine Intelligence 2020 2:10* **2**, 585–594 (2020).
41. Ronneberger, O., Fischer, P. & Brox, T. U-Net: Convolutional Networks for Biomedical Image Segmentation. *arXiv* **1505**, (2015).
42. Shit, S. *et al.* clDice -- a Novel Topology-Preserving Loss Function for Tubular Structure Segmentation. *Proceedings of the IEEE Computer Society Conference on Computer Vision and Pattern Recognition* 16555–16564 (2020) doi:10.48550/arxiv.2003.07311.
43. Park, H.-E. *et al.* Scalable and Isotropic Expansion of Tissues with Simply Tunable Expansion Ratio. *Advanced Science* **6**, 1901673 (2019).
44. Smets, G. & Hesbain, A. M. Hydrolysis of polyacrylamide and acrylic acid–acrylamide copolymers. *Journal of Polymer Science* **40**, 217–226 (1959).
45. Law, W. K. & Chung, A. C. S. Optimally oriented flux for curvilinear structure detection in volumetric images. in *10th European Conference on Computer Vision* 368–382 (LNCS, 2008).
46. Sawhney, R. & Crane, K. Boundary First Flattening. *ACM Transactions on Graphics (TOG)* **37**, (2017).

ONLINE METHODS

Mechanical configuration. MEGAtome includes two main modules: a sample mounting and feeding platform and a blade vibration generation and control mechanism. The sample mounting and feeding platform is configured through two commercial high-precision linear stages (M-531, M-511; Physik Instrumente): one stage is orientated horizontally, the other one is orientated vertically. The vertical stage is mounted on the moving piece of the horizontal stage through an L-shaped adapter bracket. A sample carrying platform, where the sample will be fixed on, is mounted on the vertical stage. A pair of linear guiding rails and bearings are configured as a passive linear stage. It is connected to the M-531 linear stage through a moving platform, on which sits the buffer solution tank (**Fig. 1b**). Thus, the large weight of the solution filled tank is stably supported by both the M-531 stage and the passive stage. When the sample is mounted, the sample is fully emersed in the buffer solution in the tank. During operation, the horizontal stage feeds the mounted sample towards the vibrating blade to realize slicing. It returns the sample to its starting position after a slice is generated; then the vertical stage elevates the sample to the next cutting position. Thickness of the slices is determined by the step distance of the vertical stage. This process is repeated until the slicing process is finished.

The blade vibration generation and control mechanism mainly include: three pairs of flexures (F_1, F_2 and F_3), a blade mounting assembly, a voice coil actuator (NCC03-15-050-2X; H2W Technologies), and two sets of laser displacement sensors (ZX2; Omron). Flexure F_1, F_2 and F_3 are thin aluminum beams that are flexible in the blade vibrating direction. Flexure F_1 connects an intermediate mass, where the vibration input is exerted, and the stationary ground. Flexure F_2 connects the intermediate mass and the blade mounting assembly, where the vibration output is expected. Flexure F_3 connects the blade mounting assembly and the station ground vertically to eliminate the out-of-plane displacement. All the flexures are machined with CNC process from 7075 aluminum alloy. The blade mounting assembly accommodates to both off-the-shelf blades and custom-made blades as long as 120 mm. The blade mounting assembly is also designed to be light weight to avoid lowering the natural frequency of the mechanism. The voice coil actuator consists of a stationary magnet and a moving coil. When given an oscillating current, an oscillating force is generated to the moving coil which is attached to the blade mounting assembly. The amplitude and frequency of the force is linear to the amplitude and frequency of the current. The laser displacement sensors are used to measure the blade vibration input and output feedback.

120 mm long blades were machined by Cadence through CNC process. The blades were made from 316 stainless steel, the blade thickness was 0.25 mm, the hone angle was 13°.

Electronic system configuration. To control the voice coil actuator, we use an I/O device (USB-6363; National Instruments) to generate analog current output signal. The signal generator is connected to a current mode driver (LCAM-5/15; H2W Technologies), which also drives the actuator. The same I/O device is used to receive analog input signal from the laser displacement sensors for feedback signal acquisition. The sensing and actuating system is controlled by a custom-developed program written in LabView. This program allows adjusting signal frequency and amplitude. We also set up two cameras (BFS-U3-13Y3M-C USB3; FLIR) to monitor the sample slicing process from top and side views.

Modeling of the vibration system. The mechanical design of MEGAtome can be modeled as a multi-DOF vibration system in its vibrating direction. Because the spring components of the system are thin metal beams, it is reasonable to assume the material damping is neglectable, the forced equation of motion for the system can be written as:

$$\begin{bmatrix} M_1 & 0 \\ 0 & M_2 \end{bmatrix} \begin{Bmatrix} \ddot{x_1} \\ \ddot{x_2} \end{Bmatrix} + \begin{bmatrix} K_1 + K_2 & -K_2 \\ -K_2 & K_2 + K_3 \end{bmatrix} \begin{Bmatrix} x_1 \\ x_2 \end{Bmatrix} = \begin{Bmatrix} F(t) \\ 0 \end{Bmatrix} \tag{1}$$

where M_1 and M_2 are moving masses, K_1 , K_2 and K_3 are stiffnesses along x-axis of flexure F_1, F_2 and F_3. $F(t)$ is the force exerted by the voice coil actuator. Given that $F(t) = F_0 cos\omega t$, the forced response can be written as:

$$\begin{Bmatrix} x_1 \\ x_2 \end{Bmatrix} = \begin{Bmatrix} X_1 \\ X_2 \end{Bmatrix} cos\omega t$$

$$\begin{Bmatrix} X_1 \\ X_2 \end{Bmatrix} = \frac{1}{A} \begin{Bmatrix} (K_2 + K_3 - M_2\omega^2)F_0 \\ K_2 F_0 \end{Bmatrix}$$

$$A = \begin{vmatrix} K_1 + K_2 - M_1\omega^2 & -K_2 \\ -K_2 & K_2 + K_3 - M_2\omega^2 \end{vmatrix} = M_1 M_2 (\omega^2 - \omega_1^2)(\omega^2 - \omega_2^2) \tag{2}$$

where ω_1 and ω_2 are the two positive eigenvalues of Equation (2), representing the first mode and second mode natural frequency. When the excitation frequency ω is close to ω_1 or ω_2, the vibration amplitude X_1 and X_2 increase significantly.

The single-DOF vibration system models of current commercial vibratomes can be divided into two categories depending on the type of blade motion guide. Vibratomes that use traditional linear bearings, e.g., the ball bearing cartridge and guide rail combination, to constrain the blade vibration usually have large moving mass and large damping, resulting in low frequency (< 60 Hz) vibration generation. The other type of vibratomes, such as Leica VT1200, adopt flexures as their linear motion guide. They can achieve relatively high frequency, such as 85 Hz. Such system consists of a moving mass *M*, and a spring component that has stiffness *K*. The forced equation of motion for the system can be written as:

$$M\ddot{x} + Kx = F(t) \tag{3}$$

Given that $F(t) = F_0 cos\omega t$, the forced response can be written as:

$$x = Xcos\omega t$$

$$X = \frac{F_0}{K(1-(\omega/\omega_0)^2)} \tag{4}$$

where $\omega_0 = \sqrt{K/M}$ is the natural frequency of the system. Amplified vibration can be achieved near the mechanism's natural frequency ω_0, however, when driven beyond ω_0, X decreases drastically. Increasing system stiffness can increase the driving frequency but lower the amplitude of the response.

Simulation of forced vibration response. Simulation of forced vibration response for both the multi-DOF and single-DOF system were performed in Python based on Equation (2) and (4). To obtain flexure stiffnesses of the mechanism, finite element simulation was performed in SolidWorks with the real geometric parameters of the flexures. The flexures of MEGAtome are 1 mm thick beams machined with 7075 aluminum alloy. The simulated K_1 , K_2 and K_3 are 27.5 N/mm, 17.8 N/mm and 20 N/mm. M_1 is 0.1 kg, including the mass of the moving coil of the actuator and the moving mass connecting to the coil. M_2 is 0.06 kg, including the mass of the blade mounting assembly. For the simulation of a single-DOF system, it is assumed that $K = K_1$, M = 0.14 kg which includes the mass of the moving coil, the blade mounting assembly, and the connecting piece between the two parts. It is assumed that F_0 = 10 N for the simulation of both multi-DOF and single-DOF system.

Characterization of MEGAtome. To characterize the blade vibration output vs input of MEGAtome, two laser displacement sensors (ZX2; Omron) were used to measure the displacement of M_1 and M_2. The sensors were mounted to the stationary ground of the machine; they were configured to emit laser beams perpendicular to the surfaces being measured. The sensors' resolution is 1.5 μm, the measurement range is ±5 mm. Same sensor was used to measure the real blade vibration output of Leica VT1200.

To characterize the blade out-of-plane displacement vs in-plane displacement of MEGA-Slicer and Leica VT1200, three high-precision capacitance probes (CPL290; Lion Precision) were used to measure out-of-plane displacement of the blade at three different locations, including the left edge, right edge, and the center of the blade. The non-contact probes detect small displacement by sensing changes of the capacitance of the electric field between the probe and the conductive object surface. The resolution of the sensors is 5 nm RMS. At the same time, a laser displacement sensor was used to measure the in-plane blade vibration. Measurements for both machines were performed with the same 80 mm-long blade (D554G50; Sturkey).

Acquisition of human and mouse tissues. Whole human brain hemispheres in formalin solution were obtained from Massachusetts General Hospital. The brains were collected and banked in accordance with approval from the local Institutional Review Board. The formalin solution was replaced with 1XPBS (using modified 10X PBS solution, pH 7.2 (2P1072, Teknova, CA, USA) with 0.02% Sodium Azide (N, NaN3, S2002, MilliporeSigma) upon arrival, and the hemispheres were stored at 4°C until use. PFA fixed female mouse brains (10 weeks old) for the brain array (Fig. 3) were purchased from Hilltop Lab Animals.

Tissue slice surface characterization. A non-contact surface profiler (Keyence, VR-5000) was used to scan the surface of tissue slices and quantify surface roughness. The profiler illuminates the slice surface with structured light beams, height variance on the surface will cause distortion to the structured light beams. When receiving the distorted reflected light beams, the profiler can recreate the surface profile and calculate surface roughness

parameters, such as Ra, meaning the average of the microscopic peaks and valleys of the surface area being measured. Surface profile figures were generated in the VR-5000 Analyzer software.

Chemicals. A SHIELD-perfusion solution[18,32] is composed of 2.5 w/v% of Polyglycerol 3-polyglycidyl ether (GE38 or P3PE, CVC Thermoset Specialties of Emerald Performance Materials, Moorestown, NJ, USA), 4% Paraformaldehyde (PFA) using a 32% solution (15714-S, Electron Microscopy Sciences, Hatfield, PA, USA) in the buffer made of 0.1 M Sodium phosphate buffer (diluting P2072, Teknova, Hollister, CA, USA) and 50 mM Sodium chloride (diluting S5845, Teknova). After vortex-mixing all the chemicals in a 50 ml conical tube, the clear supernatant was used after centrifugation for 10 minutes at 4°C and 7,200 r.c.f. A SHIELD-OFF solution is identical to the SHIELD perfusion solution, except that it does not contain PFA. A SHIELD-ON solution is a weak-base physiological buffer solution (pH~9) to trigger epoxy-based-crosslinking of biomolecules, which is made of 0.05 M Sodium carbonate (S7795, MilliporeSigma, St. Louis, MO, USA) and 0.05 M Sodium bicarbonate (S5761, MilliporeSigma). A SHIELD solution is prepared by dissolving 2 w/v% GE38 in the SHIELD-ON solution. An mELAST solution is composed of 40 w/v% Acrylamide monomers (AA, A9099, MilliporeSigma), 0.005% Bis-acrylamide crosslinkers (BisAA, 2% bis solution, 161-0142, Bio-Rad Laboratories, Hercules, CA, USA), and 0.05% VA-044 thermal initiators (27776-21-2; Wako Chemicals, Richmond, VA, USA) for 1 mm thick tissues and 0.03% VA-044 for mouse whole-organ tissues. All the reagents but VA-044 are dissolved in 0.5X PBS (phosphate-buffered saline), which is diluted from the modified 10X PBS solution, pH 7.2 (2P1072, Teknova, CA, USA) and kept at 4°C until using. The NaCh clearing solution for passive delipidation of tissues is made by dissolving 12 w/v% Cholic Acid Sodium Salt (NaCh, J13630A1, Fisher Scientific), 75 mM Lithium hydroxide monohydrate (LiOH, 43171, Alfa Aesar, Haverhill, MA, USA), 120 mM Boric acid (B6768, MilliporeSigma), 70 mM sodium sulfite (S0505, MilliporeSigma) in DIW. The SDS clearing solution for protein denaturation, hydrolysis, and destaining is made by dissolving 200 mM Sodium Dodecyl Sulfate (SDS, 75746, MilliporeSigma), instead of 12% NaCh, in the same solution. 1X PBS, 1X PBST, 1XPBSN or 1XPBSTN is made by diluting 10X PBS into DIW with or without 0.02% Sodium Azide (N, NaN3, S2002, MilliporeSigma) and 1% TritonX-100 (T, X100, MilliporeSigma). 5 v/v% Normal Donkey Serum (ab7475, abcam) is included in all the staining buffers. The SWITCH staining buffer (PBSNaCh) is made of 1X (for passive staining) or 0.1X (for pumping staining) PBS with 5% NaCh and 0.02 w/v% NaN3 and the SWITCH-final buffer is made of 0.1 or 1XPBS with 5% NaCh, 0.02 w/v% NaN3, and 1% TritonX-100. dPROTOS (RI~1.52, pH~6), a refractive index (RT) matching solution (RI~1.52, pH~7.0-7.5) is composed of 150 mL 10 w/v% 4-methoxyphenol (M18655, MilliporeSigma) in Dimethyl sulfoxide (DMSO, D8418, MilliporeSigma), 150 mL 2,2'-Thiodiethanol (TDE, 166782, MilliporeSigma), 200 mL DIW, and 150 ul 10 w/v% Triethanolamine (TEOA, T58300, MilliporeSigma). ExPROTOS2, another RI matching solution (RI~1.48, pH~9.5) is made by dissolving 480 g Iohexol, 100 ml DMSO, 150 ml TDE in 400 ml 0.1 M Tris buffer (Trizma® base, T1503, MilloporeSigma).

mELAST tissue processing. The SHIELD-cleared tissues were incubated and equilibrated in the mELAST solution in the cold room (4°C), for 1 day (1 mm thick mouse and human brain slices), 2 days (1 mm thick whole human brain coronal slice), and 4-5 days (mouse organs). For small brain tissue slices, the polymerization was conducted in a gelling cartridge made of slide glasses with plastic spacer walls matching tissue thickness (1 or 2 mm)[32]. After filling up the hole of the cartridge with the mELAST solution, tissues were submerged inside the solution completely. The top slide glass was covered and mechanically fixed with binder clips. The cartridge was placed in a 50 ml conical tube, the tube was purged with 12 psi nitrogen gas for 1 minute, and the lid was closed tightly. The tube was vertically placed on the tube rack at room temperature for 6-7 hours for gelling. Gelling mouse organs was performed using a 15 ml conical tube. The 15 ml conical tube was cut with the cap and filled with 2 ml of the mELAST solution. The SHIELD-cleared mouse organ was submerged in the solution and the tube is placed inside a 50 ml conical tube, followed by the same nitrogen purging and gelling processes with the small tissue gelling (mouse brain coronal slices, mouse organs, and cut human brain tissues). Human brain slabs were gel-embedded in an air-tight stainless gelling chamber (**Supplementary Fig. 1d**). A human brain slab equilibrated with the mELAST solution was placed on a glass plate in a container filled with the mELAST monomer solution. A top glass plate was placed over the tissue without any bubbles trapped and the two glass plates were held on each side by two stainless steel binder clips. The glass plates with the tissue were transferred to the gelling chamber. The chamber was covered with a transparent polycarbonate plate, sealed with sixteen screws, and purged with 10-12 psi nitrogen gas for 10 minutes. The gelling was conducted for 6-7 hours at room temperature. After gelling the mELAST tissue-gel was trimmed from the gel formed inside the cartridges or glass plates. To remove the unreacted thermal initiator and monomers, the tissue-hydrogel was first washed in the SDS clearing solution at room temperature for 24 hours and at 37°C for 24 hours with solution refreshments. Protein denaturation was conducted on the tissue-hydrogel by incubating in the pre-heated SDS clearing solution at 95°C for 30 minutes, followed by the hydrolysis at 80°C for 6

hours[35,43,44]. After the hydrolysis process, the tissue-gel was post-cleared with the SDS clearing solution using a tissue pump that repeatedly compresses the tissue to 1/4 of its thickness overnight. After all the processes, the tissue-gel was pumping-washed with 1% 1XPBSTN and 1XPBSN for 5-6 hours for each with several refreshments of the buffer solution. The tissue-gel was photobleached for 2 days at 4C and kept in 1XPBSN at 4C until using.

Photobleacher design and operation. The mELAST tissue-gels were photobleached to enable high signal-to-noise imaging across a wide spectrum by removing endogenous autofluorescence (e.g., lipofusion) found in human brain tissues. The photo-bleacher mainly includes a transparent acrylic chamber to contain samples, and approximately 300 white LEDs. The LEDs shine strong light to the top and bottom surfaces of the sample. Two sets of cooling fans were included to keep sample from heating by the LEDs. The post-processed mELAST tissue-gels were placed in a zip-bag filled with 1X PBSN and the bag was placed in the chamber of the photobleacher in the cold room at 4C for two days.

Tissue pump design and operation. We developed three-sized tissue pumps for compression-assisted immunostaining of mELAST tissue-gel; small (30 mm x 30 mm), medium (85 mm x 85 mm) and large (150 mm x 150 mm) (**Fig. 4g** and **Supplementary Fig. 5**). In this design, the mechanical thinning process is realized by the relative linear movement between a pump head and a flat-bottomed container that contains mELAST tissue-gels and buffer solution. During each pumping cycle, two linear actuators (maximum pushing force of 1.3 kN) move the container up towards the stationary pump head until the tissue is compressed to a certain thickness, e.g., 0.5 mm. The actuators hold the compressing position for 40 seconds and then return to the starting position. An Arduino microcontroller is programmed to control the cyclic movement of the actuators fully automatically. Considering the large lateral dimension of mELAST tissue-gel, it is important to keep the plane of the container bottom strictly parallel to the pump head plane to achieve uniform compression staining throughout the whole tissue area. Therefore, we designed an extensively long linear movement guiding mechanism to control tilting of the moving plane. To further guarantee uniform compression, we designed a mechanism that redistribute the compressing force from the actuators to evenly distributed force at the bottom of the container. Our staining experiments using the pump shows effectively uniform staining results. The machine also features adjustable pumping and retracting speed, adjustable compression thickness, and user-friendly interface. We characterized the tissue compression repeatability of the pump by measuring the displacement of the moving plane using a laser displacement sensor. The results show that when the target compression thickness was set at 0.6 mm, the pump can reach the target consistently with about 99% repeatability (**Fig. 4g**).

IASLSFM design and operation. Multicolor-Inverted Axially-Swept Lightsheet Fluorescence Microscopes (IASLSFM) is designed to accommodate tissues with large XY dimensions and capture multicolor data with simultaneous two-color imaging. Light source of IASLSFM is a multicolor laser combiner with a fiber optic output that delivers continuous wavelength light into the illumination arm of the system. The microscope is equipped with 405 nm, 488nm, 561nm, and 647nm continuous wave laser sources for acquisitions with up to four colors. A cylindrical lens shapes the beam into a sheet, and an electrically tunable lens is used to sweep the light along the propagation axis, such that the lightsheet waist is always in-focus and acquired by the rolling shutter of the camera. This creates a near-perfectly evenly illuminated optical section with consistent axial resolution and allows for high-speed line-scanning detection. Illumination and detection on these systems is achieved through pairs of objectives set up orthogonally to one another and at a 45-degree angle to the sample. These objectives can be swapped out depending on resolution and speed requirements. For full human brain slab imaging, a 2X 0.1NA objective is used to acquire at cellular resolution. These are long working distance objectives with custom dipping caps to acquire image data through up to ~12 mm of depth. During multicolor imaging, detected light from the fluorescent probes is captured and sent through a dichroic mirror which separates the longer 2 wavelengths from the shorter two wavelengths and sends them each to a dedicated camera. Color pairing is logically determined in software such that imaging is done simultaneously for 405 nm and 561 nm as a pair, and 488 nm and 647 nm as a pair. To account for chromatic shifts between different colors detected at the same focal plane, each detection arm has its own tube lens mounted to an actuator-controlled translation stage which allows for independent focusing of each color's image into its respective camera. The tissue slabs are scanned in long strips along the X-axis of the stage during acquisition. Each microscope's XY stage is a 200mm x 200mm MS-8000 from ASI with a "precision scan" X-axis, which allows very low velocity ripple during these long acquisition movements. Synchronization between the lasers, camera, tunable lens, and stage are controlled through ASI's Tiger controller and custom LabVIEW software. We also have a custom-built 400mm x 200mm XY stage assembly from ASI to allow imaging of the largest, most expanded human brain slabs which are too big for the MS8000. Calculated selection of the step size in X allows us

to acquire with a near-isotropic voxel size. The nature of the 45-degree illumination and detection relative to the sample and stage results in a coupling of the X and Z axes. Accommodating this relationship with a careful X-step-size choice enables high axial resolution as well as clean processing and visualization of the data. Voxel columns can simply be re-shuffled to convert from the 45-degree-tilted coordinate space into typical XYZ coordinate space.

Tissue surface detection and flattening. For tissue surface detection, images were first significantly downsampled to mitigate computational expense. The tissue was then segmented from the background by applying graph cut segmentation on the image. Prior to graph cut segmentation, the image intensity histogram is clipped in order to reduce background noise (minimum clipping) and reduce variance of positive signal intensities (maximum clipping), since the image channel contains both autofluorescence and immunostaining signal which far exceeds the desired autofluorescence signal. After graph cut segmentation, morphological opening with spherical element is performed to fill any potential holes in the tissue mask. Parameters for this are set manually after quickly sampling various parameter sets on subsets of the image and viewing the results. The specific parameters are (1) minimum clipping threshold, (2) maximum clipping intensity, (3) morphological opening size, and (4) graph cut smoothing parameter. In our experience, (1) and (2) are the only parameters requiring user tuning.
The top and bottom surfaces of the tissue were detected from the tissue segmentation by finding the uppermost or bottommost segmented pixel at each (*x*, *y*). To flatten the tissue, a point cloud grid is sampled from its two surfaces and triangular meshes are created from each surface point cloud. The target points in the flattened reference frame for each surface are determined using Boundary First Flattening [2], after which thin point splines (TPS) were used to define the actual image flattening transformation.

Initial approximate slab alignment. To perform initial slab alignment, matching manual anchor points are identified in the two adjacent slabs. These are typically large, easily identifiable features such as large arteries or vessels, and span the entire cut surface. An initial rigid transformation to align these anchor points is automatically calculated by minimizing the least squares error.

Automated tracing of vasculature. Images were first filtered using a custom GPU implementation of the Optimally-Oriented Flux (OOF) filter[45], which for each pixel maximizes the outward image gradient flux flow across a sphere of given scale (or radius), as given by the expression below:

$$f(\boldsymbol{x}; r, \hat{\rho}) = \int_{\partial S_r} ((\boldsymbol{v}(\boldsymbol{x}+\boldsymbol{h}) \cdot \hat{\rho})\hat{\rho}) \cdot \hat{n} dA$$

R is the scale, or radius of the sphere, $\boldsymbol{v}(\boldsymbol{x}+\boldsymbol{h})$ is the image gradient at the sphere surface centered at a given pixel location *x*, $\hat{n}$ is the normal vector to the spherical surface, and $\hat{\rho}$ is the direction of the image gradient being projected onto the sphere. In order to generate a higher response at the vessel centerline, an Oriented Flux Asymmetry (OFA) measure (as defined below) that gives a high response at curvilinear structure edges is subtracted from the OOF measure to accentuate the vascular centerlines[46].

$$s(\boldsymbol{x}; r, \hat{\rho}) = \int_{\partial S_r} \boldsymbol{v}(\boldsymbol{x}+\boldsymbol{h}) \cdot \hat{\rho} dA$$

The OOF and OFA measures can be efficiently computed by converting the integrands into a set of linear filters, and then applying the Fast Fourier Transform on the integral. For OOF, this returns $\Lambda(\boldsymbol{x}; r)$, the strongest eigenvalue response associated with the maximal flux direction and a certain radius, while for OFA, this returns $\mathrm{Q}(\boldsymbol{x}; r)$, the magnitude of the projected image gradient on the vessel cross-sectional plane (where the cross section eigenvectors are determined from the OOF computation).

$$\Lambda(\boldsymbol{x}; r) = \max_{\hat{e_i}} f(\boldsymbol{x}; r, \hat{e_i}(\boldsymbol{x}, r)) = \max_{\hat{e_i}} \lambda_i(\boldsymbol{x}; r)$$

$$\mathrm{Q}(\boldsymbol{x}; r) = \max_{r \in R} \sqrt{s^2(\boldsymbol{x}; r, \hat{e_1}) + s^2(\boldsymbol{x}; r, \hat{e_2})}$$

The filter should give the strongest response at the center of vessels and weak at the edges; since OOF gives strong responses inside vessels and OFA gives strong responses at vessel edges, the overall filter response is given by:

$$M(\boldsymbol{x}) = \max_{r \in R}\big(0, \Lambda(\boldsymbol{x}; r) - Q(\boldsymbol{x}; r)\big)$$

Segmentation of the vessels was done by performing intensity thresholding or graph-cut segmentation in parallel on different chunks of the overall image. The specific intensity threshold for a given image was chosen manually based on user parameter tuning performed on sampled regions of the image.

Feature matching and inter-slab registration. As described in detail earlier, GPU-accelerated Optimally-Oriented Flux (OOF) followed by global intensity threshold segmentation were implemented to generate a mask of the vasculature, which was followed by parallelized medial-axis thinning on the vasculature mask to extract the vessel centerlines and transform the image into a graph of nodes, edges, and endpoints. The locations of endpoints lying near the previously determined surfaces were extracted and used as features for image registration.

A custom feature descriptor was used to correctly match corresponding vasculature endpoints in both slabs. Each endpoint feature descriptor consists of the relative (*x,y*) coordinates of its *k* (user-defined parameter) 2-D nearest neighbors. The search for potential feature correspondences for a given keypoint was localized to within a certain radius *r* (user-defined). Candidate keypoint matches within the radius were determined by evaluating the distance between the feature descriptors; however, in order to be more robust to imperfect vessel endpoint detection, the descriptor similarity was computed as the shortest distance between any $n \leq k$ (a user-defined parameter) spatial nearest neighbors. For example, for $k = 6, n = 3$:

$$\boldsymbol{f_i} = [x_{i1}\ y_{i1}\ x_{i2}\ y_{i2}\ x_{i3}\ y_{i3}\ x_{i4}\ y_{i4}\ x_{i5}\ y_{i5}\ x_{i6}\ y_{i6}]$$

$$DS(\boldsymbol{f_1}, \boldsymbol{f_2}) = \min \sum_{k \in S} \sum_{j \in S} \left| (x,y)_{1j} - (x,y)_{2k} \right|^2$$

$$S = \{(1,2,3), (1,2,4), (1,2,5), \ldots (3,5,6), (4,5,6)\}$$

Where $\boldsymbol{f_i}$ represents the keypoint descriptor vector for a point i, $(x_{ij}\ y_{ij})$ is the jth nearest neighbor 2D location to the point i, $DS(\boldsymbol{f_1}, \boldsymbol{f_2})$ is the descriptor similarity between point 1 in one image and point 2 in the other image, and *S* is the set of all $P(6,3)$ nearest neighbor permutations over which we compute the descriptor similarities. A good correspondence between a pair of keypoints is determined by computing the ratio of the best and second-best descriptor similarities and thresholding at 0.9:

$$\frac{DS(\boldsymbol{f_1}, \boldsymbol{f}_{\text{closest}})}{DS(\boldsymbol{f_1}, \boldsymbol{f}_{\text{2nd-closest}})} \leq 0.9$$

To further ensure a good correspondence, matching keypoints is done in the forward direction and in the reverse direction such that the correspondence satisfies the above inequality in both images.

Random sample consensus (RANSAC) with an affine model is applied locally to filter out outlier feature correspondences, and thin plate splines interpolated from the keypoint correspondences are used to compute the nonrigid deformation from the moving to fixed surface. To make the deformation computationally scalable, the TPS were computed exactly for a regular grid and approximated by interpolating the resulting deformation field with GPU-accelerated grid interpolation.

Interslab registration accuracy can be fine-tuned by manually annotating more matching endpoints in the newly registered image, followed by outlier removal via RANSAC, and finally defining another TPS transformation.

Interslab registration using multi-channel information. The previous deformation field defined with vasculature features can be applied to warp other image channels. The above procedure for registering images can be applied to other channels to achieve finer resolution warping if using axon endpoint features. Specifically, axon endpoints can be detected automatically or manually and a new TPS transformation can be defined to further fine-tune the registration.

Automated axon tracing.

Network structure. The U-Net architecture consists of convolutional layers interspersed with downsampling to form sequentially lower-resolution modules in an encoder path, followed by upsampling to restore the original resolution in a decoder path, with lateral skip connections between same resolution encoder and decoder modules. We used 3×3×3 convolutional layers followed by group normalization and exponential linear units. Summation joining was chosen for skip connections with an additional skip connection between the first and last convolutional layer in each module. We also used strided 2×2×2 max-pooling for downsampling, and strided transpose convolutions with max-pooling for upsampling. In our baseline approach, we trained a residual 3D U-Net with 4 resolution blocks to perform voxelwise classification using binary cross entropy loss between the output and training images. The resulting segmentation was then binarized using a threshold of 0.5, and skeletonized using morphological thinning to obtain a single voxel wide centerline. To improve upon the baseline, we replaced binary cross entropy with an alternative loss function, centerline-Dice (clDice), which incorporates parameter-free skeletonization directly into the training procedure.

Training details. Each network was trained via stochastic gradient descent using the ADAM optimizer with an initial learning rate of 1×10−4 and weight decay of 1×10−3. For training, mini batches of 16 samples were randomly

cropped from the input dataset, and augmented using random grayscale perturbations, random 90-degree X-Y rotations, and random flipping. For inference, samples were cropped using a sliding window with 50% overlap and blended using a 3D Hann window to minimize segmentation errors along the edge of the receptive field. We also incorporated test-time augmentation, by averaging predictions across 16 transformations for each input sample (unique combinations of X-Y 90 degree rotations and flipping along each axis). Test time augmentation has been shown to improve segmentation performance at the expense of a linear increase in inference time. For each model, training proceeded until convergence or until no improvement in validation loss was observed over a period of 100 epochs.

FIGURE LEGENDS

Fig. 1 | Integrated pipeline for multi-scale proteomic interrogation of the human brain. a, The workflow of the experimental pipeline for slicing, processing, immunostaining, and imaging of the human brain. After MR imaging, human brain hemispheres are sliced into mm-thick coronal slabs using MEGAtome. The slabs are SHIELD-processed and transformed into mELAST tissue-hydrogel. The tough, elastic and size-adjustable mELAST tissue-hydrogels are repeated immunostained and imaged at different physical sizes with various magnification objectives to extract high-dimensional features at multiple scales. **b**, 3D multi-scale profiling of human brain captures brain-wide structures, cytoarchitecture and local circuitry (single cell resolution imaging), cellular and subcellular phenotype (super-resolution imaging) from the same tissue.

Fig. 2 | Mechanical design and characterization of MEGAtome. a, MEGAtome consists of two main modules: a blade vibration generation and control platform (in red frame), and a sample mounting and feeding platform (in blue frame). **b**, The sample mounting and feeding platform is configured through two linear stages (LS). **c**, MEGAtome can continuously and smoothly slice whole human brain hemispheres, and large arrays of mouse brains. **d-e**, Mechanical design of the blade vibration generation and control mechanism shown in 3D view (**d**), and in XY plane (**e**). The mechanism mainly consists of 3 pairs of flexures (F_1, F_2, and F_3) and a blade mounting assembly (BMA). A voice coil actuator (VCA) drives the mechanism with oscillating force in X direction. Two laser displacement sensors (LDS) are used to measure the vibration input and output displacement. **f**, Common commercial vibratomes (such as Leica VT1200) are designed based on the single degree of freedom (DOF) mass-spring vibration model (left), MEGAtome is designed based on a multi degree of freedom vibration model (right), in which K_1, K_2, K_3 represents the stiffnesses of F_1, F_2, and F_3, respectively. M_1 represents the mass where the driving force F is applied to, its displacement x_1 is measured by LDS1. M_2 represents the mass of the blade and blade mounting assembly, its displacement x_2 is measured by LDS2. **g**, Simulation results of forced vibration response of a single DOF system, where blade vibration amplitude decays to minimal value as the driving frequency increases, and a multi DOF system, where high blade amplitude can be achieved at high frequency due to a second resonant mode. **h**, Measurements of x_1 and x_2 show that the first and second resonant mode of the mechanism occur near 80 Hz and 140 Hz. **i**, Measurements of blade vibration output versus vibration input of Leica VT1200 vibratome and MEGAtome. **j**, Demonstration of ideal blade vibration and real blade vibration which is accompanied with parasitic errors. Three high-precision capacitance probes (CP) are used to measure blade parasitic vibration displacement. **k**, Measurements of blade out-of-plane parasitic vibration amplitude versus in-plane vibration amplitude of Leica VT1200 vibratome and MEGAtome. **l**, MEGAtome generated 1mm, 200 μm, and 100 μm slices from whole human cerebellums (top row). Leica VT1200 failed to generate complete slices at its maximum vibrating speed (bottom row). The 1 mm – thick slices were scan by an optical profiler showing the surface height variance (Methods). For whole slice figures, scale bar=10 mm; for enlarged figures, scale bar=2 mm.

Fig. 3 | MEGAtome slicing of whole human brain hemisphere and array of mouse brains. **a-d**, A banked human brain hemisphere (**a**) was embedded in gel (**b**) and then sliced by MEGAtome into 40 consecutive 4 mm-thick uniform slices that kept complete tissue from the hemisphere (**c, d**). **e**, To gel-embed a whole human brain hemisphere, liquid gel is first poured onto the hemisphere in a custom-designed container that has detachable walls; after gel becomes solidified, walls of the container are detached, the gel is brought to be submerged in PFA solution. After sufficient fixation is formed between tissue and gel, the hemisphere is mounted onto the vibratome for slicing. **f**, NeuN+ neurons were imaged in 4 mm thick SHIELD human brain coronal slab that contains multiple cortex regions, hippocampus, striatum and thalamus. **g**, 3D rendering, enlarged xy plan views of NeuN+ cells from each brain region. **h**, Custom-designed embedding tools allow for gel embedding and vibratome slicing at least 35 brains (per area of 72 mm x 80 mm) together. **i**, Gel embedding process of mouse brain arrays starts with liquid gel being poured to the assembled tools. **j**, The mouse brain-shaped placeholders allow the gel to form fitted cavities to hold all brains in the same coronal position. **k**, More liquid gel is poured to fully immerse the brains. **l**, The solidified gel and brain mixture is fixed in PFA solution. **m**, MEGAtome generated consecutive, uniform slices from an array of 35 mouse brains that were embedded together in gel, enabling high-throughput imaging of neurons. **n**, Marmoset hemisphere-shaped placeholders were designed based on the surface scan of a left marmoset hemisphere. Array of 6 marmoset hemispheres were embedded and sliced together following the same protocol as mouse brain array embedding and slicing. Scale bar, 10 mm.

Fig. 4 | Integrated tissue transformation and staining pipeline for 3D multi-scale molecular imaging of the human brain. a-c, mELAST technology transforms intact human brain tissues into a transparent, permeable, tough-elastic, and size-adjustable material. **a**, The photos show the processing workflow of a human brain coronal slab. Scale bar, 3 cm. **b**, mELAST human brain tissue-hydrogels are highly elastic and linearly expands 4-5x in water. Scale bar, 1 cm. **c**, Size-adjustability of PFA tissues and mELAST tissue-gels are compared in dPROTOS (an RI matching media) and water. L0 is mean length of original brain. L is mean length in dPROTOS or water. **d**, A photobleaching device removes autofluorescence from lipofuscin and other autofluorescing pigments in human brain tissue. **e**, Photobleaching allows for high signal-to-noise imaging. **f**, Mean background signal values of SPIM images before and after photobleaching (in **e**) are compared. **g**, A large human-brain-scale tissue pump was developed for accelerated immunolabeling of large-scale mELAST tissue-gels. An mELAST tissue-gel is placed in a chamber with buffer solution and repeatedly compressed for clearing, washing, staining, and destaining. A graph of the measurement of the gap between the pump head and the chamber floor when the pump is operated repeatedly shows the accuracy. **h**, SWITCH-pumping staining allows rapid, uniform, and cost-effective immunostaining of mELAST tissue-gels. Three same-sized mELAST human brain tissue-gels were stained with POPO1 (Nuclei dye), a-PV, and a-NFH antibodies using passive, pumping and SWITCH-pumping methods, and the staining uniformity is compared **i-j**, 3D multi-scale imaging of volumetric tissues. **i**, IASLSFM, a rapid, oblique-operated, and multi-color light sheet microscopy allows imaging of large-scale tissues. **j-k**, SWITCH-pumping labeling and IASLSFM imaging methods allow for single cell resolution imaging of intact human brain coronal slab and single-axon resolution imaging of axonal fibers (a pan-axonal marker) in an 3x expanded mELAST human brain tissue-gel. The images were obtained with a 2x/0.1NA objective (**e**-upper images**, j**), a 20x/0.5NA objective (**e**-lower images, **h**), and a 16.7x/0.4NA objective (**k**).

Fig. 5 | Multiplexed, multi-scale proteomic phenotyping of control and AD human brain tissues. a, NeuN+ (a pan-neuronal marker) and IBA1+ (a microglia marker) cells were stained and imaged in 2 mm thick SHIELD-processed control and Alzheimer Disease (AD) human brain coronal slabs that contain prefrontal cortex (A9m), orbitofrontal cortex (A11m), and cingulate neocortex (MFC). The images show different atrophy and cell number density between control and AD. **b-f**, mELAST enables multiplexed imaging and phenotyping. **b**, Multiplexed staining and imaging of an mELAST human brain tissue-gel from prefrontal cortex (A10 frontal polar cortex). The mELAST tissue-gel was subject to repeated

SWITCH-pumping staining, destaining, and multi-round imaging using IASLSFM. Round 1: YOYO1, NeuN (NeuN), Lectin, Round 2: YOYO1, Calretinin (CR), Somatostatin (SST), Round 3: YOYO1, Parvalbumin (PV), Ionized calcium binding adaptor molecule 1 (IBA1), Round 4: YOYO1, Neuropeptide-Y (NPY), and Glial fibrillary acidic protein (GFAP). **c**, The enlarged view shows the spatial distribution of multiple cell types in 3D in the prefrontal cortex of the normal human brain. Scale bar, 200 µm. **d,** Comparison of number density and distribution of CR+ cells in the control and AD mELAST tissue-gels. **e-f**, Comparison of number density of NeuN+, IBA1+ (**e**) CR+, SST+, PV+, and NPY+ (**f**) cells in the control and AD mELAST tissue-gels. **g-j**, mELAST enables supperresolution imaging. **g**, 3D micro-environment and fine cell morphologies are captured in expanded mELAST tissue-gels. Scale bar, 25 µm (100 µm in expanded). An IBA1+ microglia was reconstructed in 3D with AD hallmarks (ABETA Plaque and PTAU fibers). **h-i**, 3D mapping of Synapsin I/II (a presynaptic marker) and PSD-95 (a postsynaptic marker) in expanded control and AD mELAST human brain tissue-gels. Scale bars, 5 µm and 0.5 µm (20 µm and 2 µm in expanded). **j**, Comparison of number density of Synapsin I/II and PSD95 in the control and AD mELAST tissue-gels (total volume and inside ABETA plaques). The images were obtained with a 2x/0.1NA objective (**a-d**), a 20x/0.5NA objective (**g**), and a 63x/1.2NA objective (**h-i**). The number density of cells and synapses in AD tissue (**d, e, and j**) was normalized by 2.2 to account for different degrees of atrophy. Anatomical annotations in **a,b** from Allen Brain Reference Atlases (Adult Human, Modified Brodmann), http://atlas.brain-map.org[16].

Fig. 6 | Computational pipeline enables accurate interslab registration to reconstruct sliced tissue blocks and semi-automated tracing of densely packed axons. a, Projectome mapping of large intact tissue requires separate processing, staining, and imaging of sliced mm-thick slabs followed by computational reconstruction, axon tracing, and downstream analysis. **b**, Macro-scale interslab registration pipeline (HuBRIS) at vasculature registration involves first flattening the surfaces, preliminarily rigidly aligning the slabs using manually selected anchor points, and then nonrigid deformation based on feature matching between geographically similar vessel endpoints. **c**, Axon resolution registration is achieved by starting with the vasculature-registered slabs, and then using finer features such as astrocytic processes or neural axonal fibers to achieve progressively finer scale registration. **d**, Deep-learning based axon tracing algorithm performs end-to-end detection of axon centerlines by using a residual 3D U-Net architecture that directly utilizes centerline DICE score (clDICE) as loss function.

Fig. 7 | Multiplexed uniform staining and axonal resolution imaging enables macroscopic (vasculature resolution) and microscopic (single fiber resolution) registration and axonal connectivity mapping in human cortical tissue. a, Using lectin, two cortical human tissue slabs can be interslab-registered to single vessel resolution, providing a groundwork for fine-tuning using the other neural fiber channels. Scale bars, 1 mm. **b-e**, Demonstration of NFH and GFAP registration at single axonal fiber resolution within a single field of view of the larger cortical tissue, depicting NFH in pre-registration, after vasculature registration, after fine-tuning using PV/GFAP fiber endpoints, and after fine-tuning using NFH endpoints Scale bars, 0.1 mm. **b**, Inset, xz and xy NFH and GFAP maximum intensity projections (MIP) of one field of view within the slabs. **c**, After using the coarse macroscale lectin registration parameters used to achieve vasculature resolution registration demonstrated in (A), NFH+ axons can nearly be connected through the slabs. **d**, NFH axonal fibers and astrocytic fibers can be easily connected by eye after registration using PV+ and GFAP+ fiber endpoints. **e**, NFH+ axons and GFAP+ fibers are nearly perfectly connected through consecutive tissue slabs after fine-tuning the registration with NFH endpoints. **f**, Histogram of absolute errors for NFH axonal fibers during each step of the registration process (vasculature registration, PV/GFAP fine-tuning, NFH fine-tuning). **g**, X-Y lateral connectivity errors for NFH axonal fibers during each step of the registration process (vasculature registration, PV/GFAP fine-tuning, NFH fine-tuning). **h**, Fibers in a small inset of the field of view can be connected increasingly well using multi-channel registration. **i**, YZ max intensity projection of NFH in

interslab registered slabs with detected axon centerlines overlaid (gray; scale bar, 20 μm). (i)-(ii) Zoomed in insets showing automatically traced axons spanning both slabs (scale bars, 10 μm).

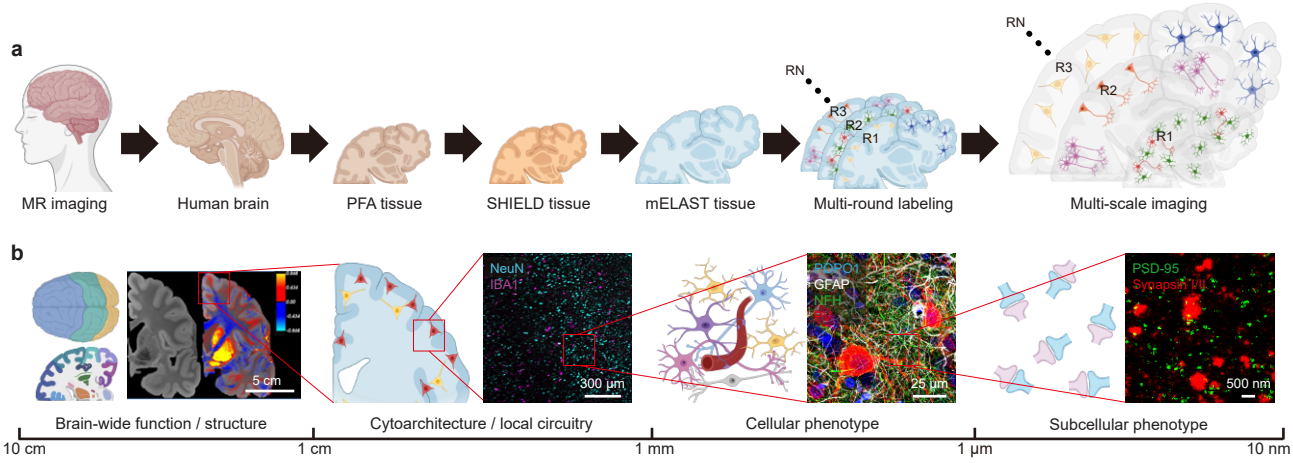
a
MR imaging
Human brain
PFA tissue
SHIELD tissue
mELAST tissue
RN
R3
R2
R1
Multi-round labeling
RN
R3
R2
R1
Multi-scale imaging
b
5 cm
NeuN
IBA1
300 μm
PDPO1
GFAP
NFH
25 μm
PSD-95
Synapsin I/II
500 nm
Brain-wide function / structure
Cytoarchitecture / local circuitry
Cellular phenotype
Subcellular phenotype
10 cm
1 cm
1 mm
1 μm
10 nm

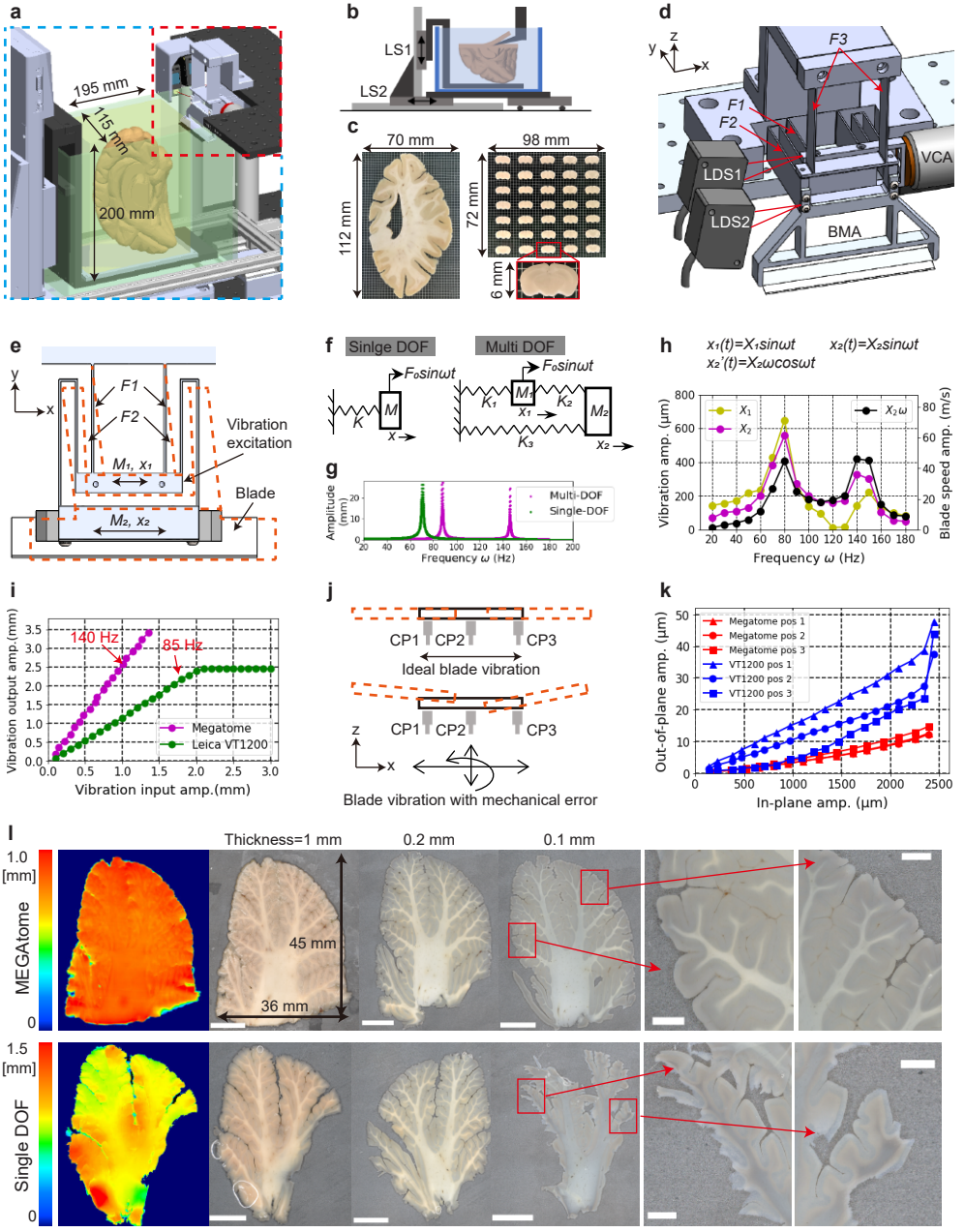
a
195 mm
115 mm
200 mm
b
LS1
LS2
c
70 mm
98 mm
112 mm
72 mm
6 mm
d
F3
F1
F2
VCA
LDS1
LDS2
BMA
e
F1
F2
Vibration excitation
Blade
f
Sinlge DOF
Multi DOF
g
Multi-DOF
Single-DOF
Frequency ω (Hz)
h
Vibration amp. (μm)
Blade speed amp. (m/s)
Frequency ω (Hz)
i
140 Hz
85 Hz
Megatome
Leica VT1200
Vibration output amp.(mm)
Vibration input amp.(mm)
j
CP1
CP2
CP3
Ideal blade vibration
Blade vibration with mechanical error
k
Megatome pos 1
Megatome pos 2
Megatome pos 3
VT1200 pos 1
VT1200 pos 2
VT1200 pos 3
Out-of-plane amp. (μm)
In-plane amp. (μm)
l
Thickness=1 mm
0.2 mm
0.1 mm
45 mm
36 mm
MEGAtome
Single DOF

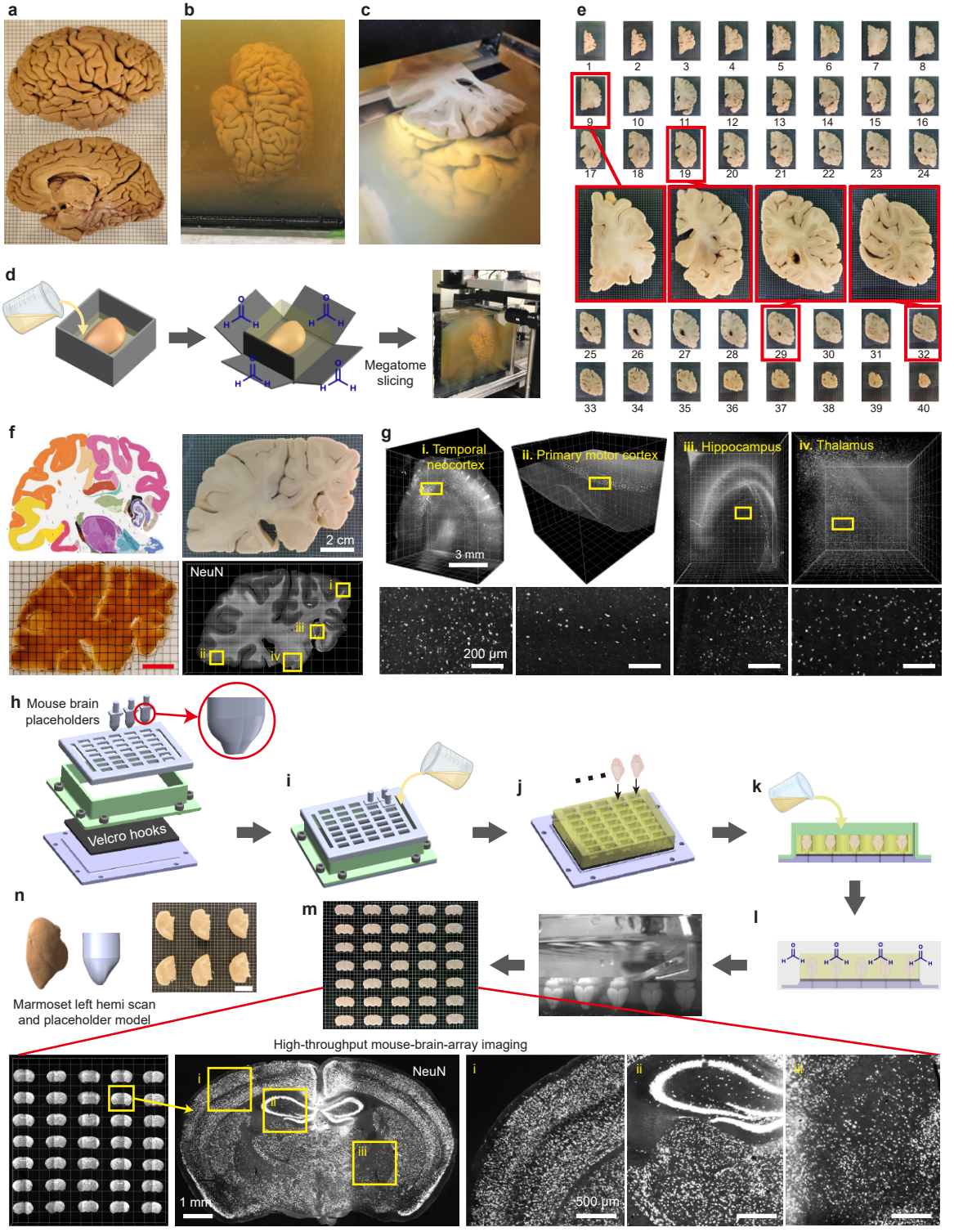
a
b
c
e
d
Megatome slicing
f
2 cm
NeuN
i
ii
iii
iv
g
i. Temporal neocortex
ii. Primary motor cortex
iii. Hippocampus
iv. Thalamus
3 mm
200 µm
h Mouse brain placeholders
Velcro hooks
i
j
k
l
m
n
Marmoset left hemi scan and placeholder model
High-throughput mouse-brain-array imaging
NeuN
1 mm
500 µm

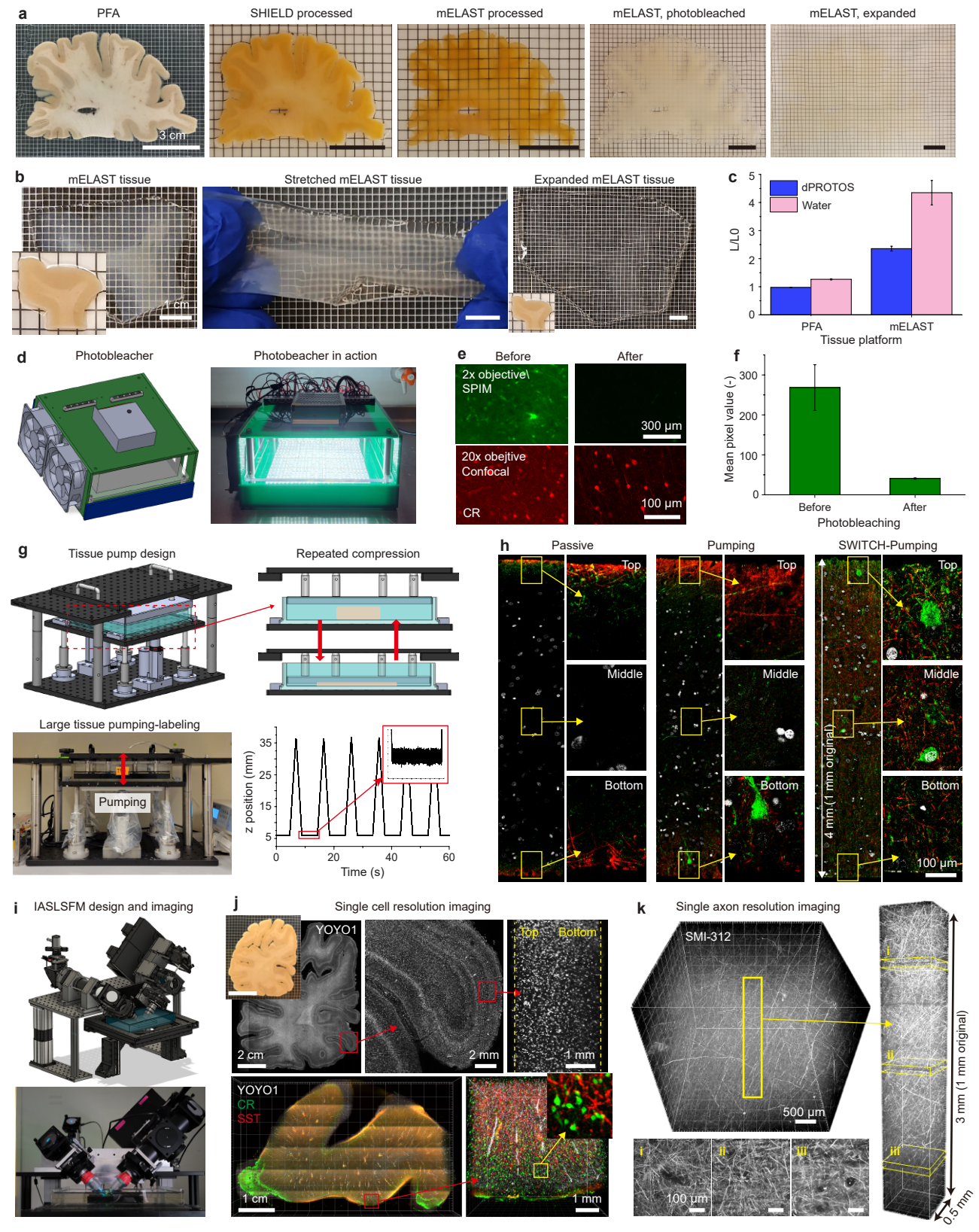
a
PFA
SHIELD processed
mELAST processed
mELAST, photobleached
mELAST, expanded
3 cm
b
mELAST tissue
Stretched mELAST tissue
Expanded mELAST tissue
1 cm
c
dPROTOS
Water
L/L0
PFA
mELAST
Tissue platform
d
Photobleacher
Photobeacher in action
e
Before
After
2x objective\
SPIM
300 µm
20x obejtive
Confocal
CR
100 µm
f
Mean pixel value (-)
Before
After
Photobleaching
g
Tissue pump design
Repeated compression
Large tissue pumping-labeling
Pumping
z position (mm)
Time (s)
h
Passive
Pumping
SWITCH-Pumping
Top
Middle
Bottom
4 mm (1 mm original)
100 µm
i
IASLSFM design and imaging
j
Single cell resolution imaging
YOYO1
2 cm
2 mm
1 mm
Top
Bottom
YOYO1
CR
SST
1 cm
1 mm
k
Single axon resolution imaging
SMI-312
500 µm
100 µm
3 mm (1 mm original)
0.5 mm

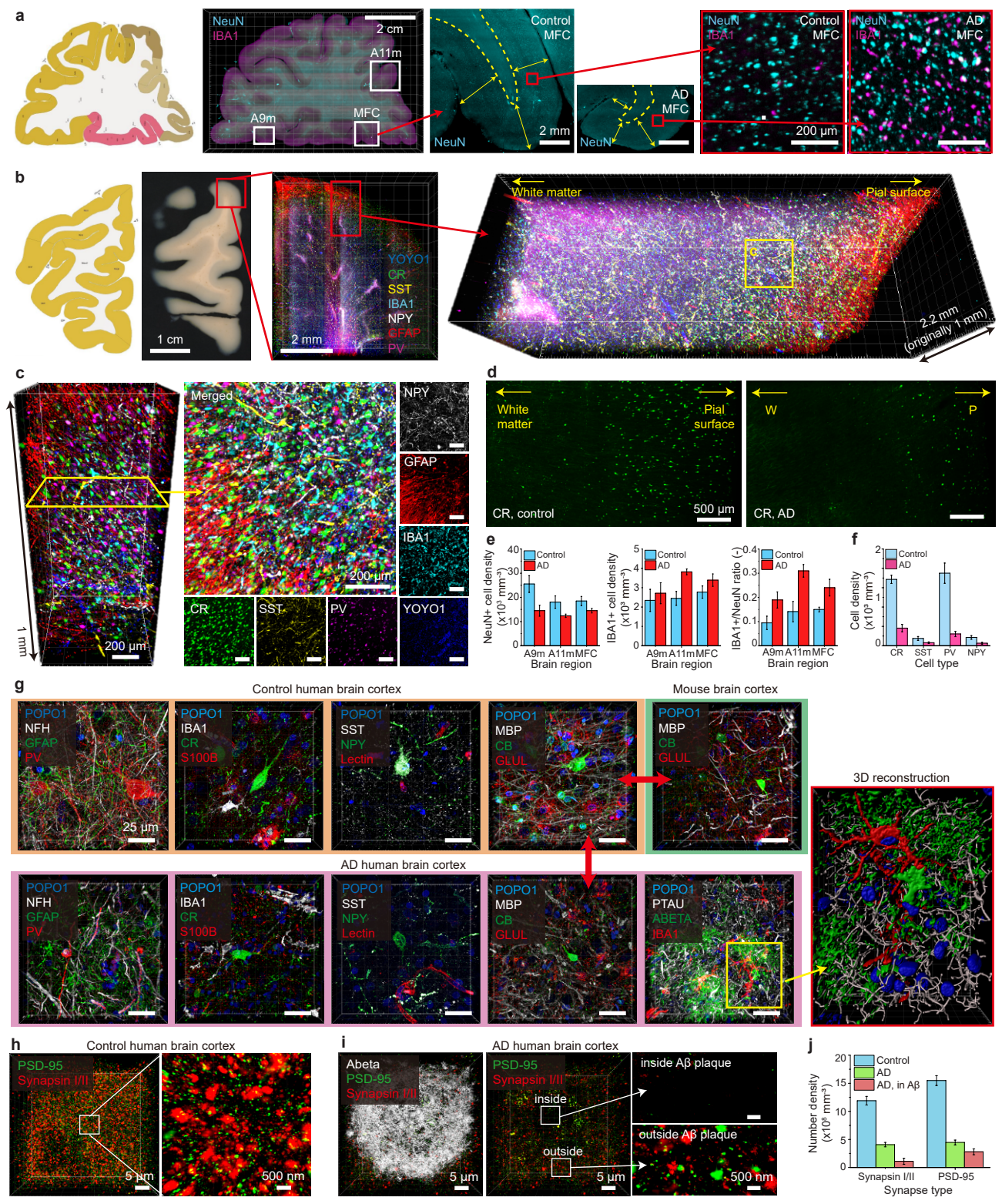
a
NeuN
IBA1
2 cm
A11m
A9m
MFC
Control
MFC
2 mm
NeuN
AD
MFC
200 µm
b
1 cm
2 mm
YOYO1
CR
SST
IBA1
NPY
GFAP
PV
White matter
Pial surface
c
2.2 mm
(originally 1 mm)
c
Merged
NPY
GFAP
IBA1
200 µm
CR
SST
PV
YOYO1
1 mm
200 µm
d
White
matter
Pial
surface
CR, control
500 µm
W
P
CR, AD
e
Control
AD
NeuN+ cell density
(x10³ mm⁻³)
IBA1+ cell density
(x10³ mm⁻³)
IBA1+/NeuN ratio (-)
A9m A11m MFC
Brain region
f
Control
AD
Cell density
(x10³ mm⁻³)
CR SST PV NPY
Cell type
g
Control human brain cortex
Mouse brain cortex
3D reconstruction
AD human brain cortex
POPO1
NFH
GFAP
PV
IBA1
CR
S100B
SST
NPY
Lectin
MBP
CB
GLUL
PTAU
ABETA
25 µm
h
Control human brain cortex
PSD-95
Synapsin I/II
5 µm
500 nm
i
AD human brain cortex
Abeta
PSD-95
Synapsin I/II
5 µm
inside
outside
inside Aβ plaque
outside Aβ plaque
500 nm
j
Control
AD
AD, in Aβ
Number density
(x10⁸ mm⁻³)
Synapsin I/II
PSD-95
Synapse type

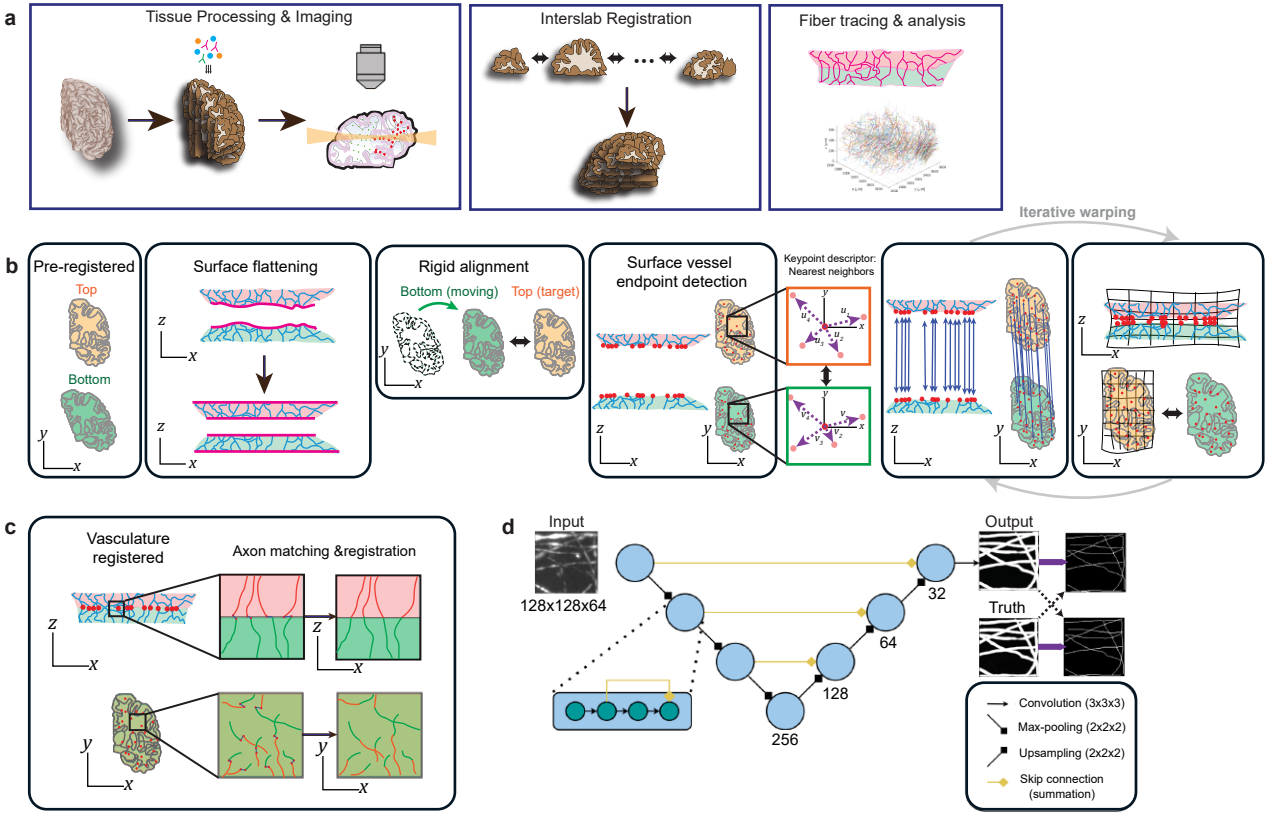
a
Tissue Processing & Imaging
Interslab Registration
Fiber tracing & analysis
b
Pre-registered
Top
Bottom
Surface flattening
Rigid alignment
Bottom (moving)
Top (target)
Surface vessel endpoint detection
Keypoint descriptor: Nearest neighbors
Iterative warping
c
Vasculature registered
Axon matching &registration
d
Input
128x128x64
Output
Truth
32
64
128
256
Convolution (3x3x3)
Max-pooling (2x2x2)
Upsampling (2x2x2)
Skip connection (summation)

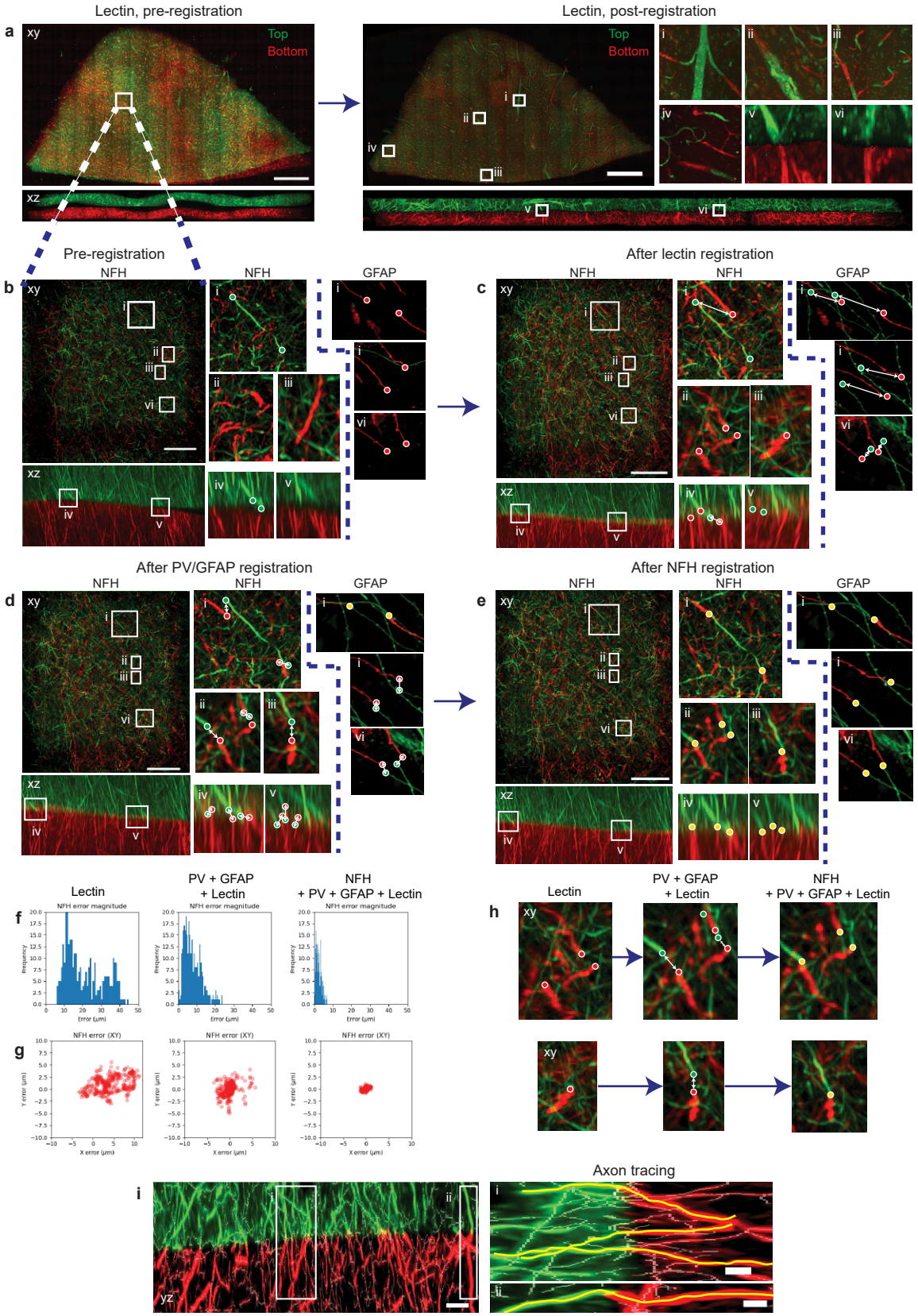
Lectin, pre-registration
Lectin, post-registration
a
xy
xz
Top
Bottom
Pre-registration
After lectin registration
After PV/GFAP registration
After NFH registration
b
c
d
e
NFH
GFAP
f
g
h
Lectin
PV + GFAP
+ Lectin
NFH
+ PV + GFAP + Lectin
NFH error magnitude
Frequency
Error (µm)
NFH error (XY)
X error (µm)
Y error (µm)
i
yz
Axon tracing